Piezoelectric Force Microscopy study on Zinc Tin Oxide Nanowires

Relatore:

Prof. ssa Beatrice Fraboni

Correlatore:

Dott. Tobias Cramer

Presentata da:

Klein Tahiraj

Për mamin

dhe babin.

Sommario

Piezoelectric force microscopy study on zinc tin oxide nanowires

Di Klein TAHIRAJ

I sensori autoalimentati potrebbero trovare un'ampia applicazione per monitorare la salute personale, le automobili o gli edifici. Una delle forme più onnipresenti di energia su cui questi dispositivi potrebbero fare affidamento è l'energia vibrazionale. Per convertire questa energia in energia elettrica, la ricerca si sta concentrando sui materiali piezoelettrici. Esempi di questi materiali, sono gli ossidi di zinco-stagno (*ZTO*). Questi ultimi, modellati in nanofili e incorporati in un elastomero di silicio presso i laboratori dell'Università di Lisbona, hanno dimostrato di produrre una conversione energetica macroscopicamente efficiente. In questo lavoro uso la Microscopia a Forza Piezoelettrica per caratterizzare la risposta piezoelettrica di un singolo nanofilo di *ZTO*, cioè per misurarne componente d_{33} del tensore di deformazione piezoelettrica. Il *P(VDF-TrFE)* in film sottile, ovvero un materiale con proprietà piezoelettriche ben caratterizzate, viene utilizzato per calibrare la sensibilità dello strumento. Il valore che ottengo per il d_{33} del nanofilo di *ZTO* è $23.70 \pm 0.04 pm/V$. Una caratterizzazione per un nanofilo ZnO viene inoltre effettuata con l'obiettivo di usarla come riferimento. Il valore che ottengo è di $10.36 \pm 0.03 pm/V$. Il valore per il nanofilo di ZTO risulta dunque essere circa il doppio di quello dello ZnO. Questo risultato certifica i nanofili di ZTO come buoni candidati per la conversione di energia nei futuri dispositivi autoalimentati.

Abstract

Piezoelectric force microscopy study on zinc tin oxide nanowires

by Klein TAHIRAJ

Self-powered sensor devices could find widespread application to monitor personal health, automobiles or buildings. One of the most ubiquitous form of energy on which these devices could rely is vibrational energy. To convert this energy into electrical energy, the research is focusing on piezoelectric materials. Examples of these materials are *ZnO* or Zinc Tin Oxides (*ZTO*). Modelled into nanowires and incorporated into an elastomer at the University of Lisbon, these materials have been demonstrated to result in macroscopically efficient energy conversion. In this work, I use Piezoelectric Force Microscopy to characterize the piezoelectric response of a single *ZTO* nanowire, namely, to measure the component d_{33} of its piezoelectric strain tensor. P(VDF-TrFE) thin film, i.e. a material with well characterized piezoelectric proprieties, is used to calibrate the instrument sensitivity. The value I obtain for the d_{33} of the *ZTO* nanowire is $23.70 \pm 0.04 pm/V$. In order to use it as a reference, I perform a characterization also to a *ZnO* nanowire. The value I obtain is $10.36 \pm 0.03 pm/V$. The value for the ZTO nanowire is therefore about double that of the ZnO. This result certifies ZTO nanowires as good candidates for energy conversion in future self-powered devices.

Table of Contents

Introduction

Self-powered sensor devices could find widespread application to monitor personal health, automobiles or buildings, providing information that could help to improve our security and well-being as well as to reduce our environmental impact[1,2]. Self-powered sensor devices rely on an energy source other than batteries or power cords. With the appropriate technologies, energy from chemical reactions, but also from thermodynamic or mechanic processes, can be converted into electrical energy. One of the most ubiquitous forms of energy to be harvested by self-powered devices is vibrational energy. Indeed, our world is constantly affected by continuous vibrations and motions. The ground, for example, even if it is not easily perceived, vibrates constantly[3]. Also, the sounds that we hear, are nothing more than vibrations of the fluids that surround us. Thus, the human body is also continuously affected by vibrations and motions. The ability to transform mechanical vibrational energy into electrical energy is what can open the door to the new technologies of the future. One of the best-performing methods for obtaining energy from vibrations is to exploit the phenomenon of piezoelectricity. The deformation of a piezoelectric material is proportional to the electric field applied, and vice versa. In the general case, this proportionality is expressed by a tensor. The magnitude of the tensor elements then describes the efficiency of a material for electromechanical energy conversion. In recent years it has been demonstrated that nanostructured piezoelectric materials have particularly large piezoelectric coefficients and can be tailormade to be included in soft piezoelectric composites for energy-harvesting devices[4–7]. An example are ZnO or $ZTO-bases$ nanowires incorporated into a silicone elastomer as fabricated in recent progress at the University of Lisbon. Such materials have been demonstrated to result in macroscopically efficient energy conversion able to power small LEDs[8]. However, a detailed characterization of the piezoelectric response of the single nanomaterial is still missing and is crucial to understand the operation mechanism and performance of the energy harvester. In this work, I will address this task by performing piezoelectric force microscopy on ZnO and $ZnSnO_3$ produced in the laboratories of the Materials Science department of the NOVA University of Lisbon. The objective is to determine the d33 element of the piezoelectric tensor of single nanowires.

In Chapter 1, an introduction to the phenomenon of piezoelectricity is presented. Starting from its discovery in 1880, we describe first the properties of dielectrics, of which piezoelectric

materials are a subclass, and then we offer an explanation of the phenomenon of piezoelectricity. Then the material to be characterized and the two used as reference standards. *ZnO* is a material of the same class of the $ZnSnO_3$ and is therefore used as a comparison. *PVDF-TrFE*, on the other hand, has been studied for a long time and its piezoelectric properties are well known. Therefore, it is used as an absolute reference for the calibration of the instrument used for measurements. Finally, a more complete presentation of the applications of $ZnSnO_3$ and *ZnO* is presented. In Chapter 2, the equipment used for the measurements is described, i.e. the NX10 Scanning Probe Microscope of the Park System Corp. Starting from a general description of its functioning, the main techniques that will be used for the characterization of the various materials are then explored. Chapter 3, on the other hand, is dedicated to the discussion of the data collected. Starting from the images reworked with *Gwydionn*, the piezoelectric properties of *PVDF-TrFE* are first verified. Then, fixing the value of the d_{33} of the latter to that known from the literature, the value of the sensitivity of the instrument is calculated. Then we move on to the characterization of the piezoelectric properties of the $ZnSnO_3$ and *ZnO* calculating the value for their d_{33}. At the end, in the conclusion part, we compare the obtained d_{33} values and resume the whole work.

1 Chapter 1 – Theoretical Background

Piezoelectricity is the accumulation of electric charge on a solid material's surface in response to a mechanical stress. Its first observation was made in 1880 by the French physicists Jacques and Pierre Curie, who demonstrated that pressure on quartz and topaz crystals produces electric currents[9]. Today the definition also includes the deformation of certain solids under the influence of an external electric field. This latter phenomenon is precisely called *the inverse piezoelectric effect* and was deduced mathematically from thermodynamic principles by Gabriel Lippmann in 1881[9]. Figure 1.1 shows a schematic diagram of the piezoelectric effect[10]. The term piezoelectricity arises from the analogy with the earlier know phenomenon of ferroelectricity, where the prefix *piezo-* is borrowed from the Greek word πιέζειν (*piezein)*, which means to press[9]. Piezoelectric materials present a broad set of electromechanical proprieties that lead to interesting applications. For instance, historically one of the first applications was an ultrasonic submarine detector, developed by the French physicist Paul Langevin during the World War I[11]. Nowadays, piezoelectric materials are exploited for a large variety of precision applications. This applications includes actuators[12], pressure sensors[13], underwater acoustic[14], drug delivery in therapies[15] and energy harvesting[16]. In the following I will provide a detailed introduction on the physical principles underlying the piezoelectric effect.
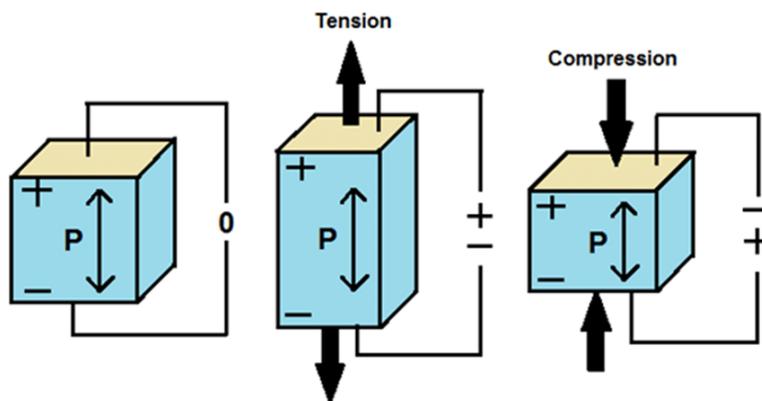

Figure 1.1: Piezoelectric effect diagram, direct and inverse piezoelectric effect.

1.1 Theoretical Notions

1.1.1 Dielectrics and Electric Polarization

All piezoelectric materials are a subset of dielectric materials, to understand the proprieties of the former, is so necessary to start from a model of the latter. A dielectric is an electrical insulator material that can be polarized by the application of an electric field. When a dielectric material is placed in an electric field, because the covalent bonds are strong enough to keep the electrons in place, it does not exhibit a flow of charges as happens for metals. Indeed, only local displacements of electrons and of the atomic nuclei happen, resulting in a net deformation of the material through the so-called *dielectric polarization phenomena*. Because of this net deformation, the material undergoes change in its dimensions. The magnitude of this change depends upon the crystal class to which the dielectric belongs. Among the 32 crystal classes, 21 are non-centrosymmetric, i.e. do not possess a centre of symmetry, while 11 are centrosymmetric, i.e. do possess a centre of symmetry. When a non-centrosymmetric dielectric is subjected to an external electric field, because of its structure, the movements of the neighbouring ions lead to significant deformations of the crystal. When this happens, the material is called *piezoelectric*. Instead, when a centrosymmetric dielectric is subjected to an external electric field, the displacement of cations and anions get cancelled because of the symmetric structure. Here, the net deformation is ideally nil. However, because of the anharmonicity of real bonds, a small second order deformation arises. This deformation has the name of *electrostrictive effect.* It must be said that because all dielectrics have non-perfectly harmonic bonds, the electrostrictive effects affects all of them. This means that also the piezoelectric material undergo the electrostrictive effect, but it get masked by the magnitude of the piezoelectric effect[17]. A second classification for dielectrics starts from their charge distribution. We call *nonpolar* dielectrics materials whose centres for positive and negative charges do coincide. P*olar dielectrics are instead* dielectrics in which opposite charge centres do not coincide. Under the influence of an external electric field, in the former type, the centres of the positive and negative charges get separated and an *induced dipole moment* is generated, while in the latter the native dipole moment is subjected to a reorientation in the direction of the field.

Taking into account only electrostatic interactions, atoms and molecules can be described by an electric charge distribution $\rho : \rho(x, y, z)$. This distribution is a function of the spatial

coordinates and is positive where the nuclei are and negative where the electrons are. The electric field generated by the distribution at distant points can be computed as $-\boldsymbol{\nabla}\phi$. The term ϕ is the electric potential of the distribution, namely:

$$\phi = \frac{1}{4\pi\epsilon_0} \int \mathrm{d}v' \frac{\rho(x',y',z')}{R} \tag{1.1}$$

with $\mathrm{d}v'$ as a volume element of the distribution and ϵ_0 as the vacuum permittivity. For non-trivial distributions, the expression of the potential can be obtained from symmetry arguments as a series called *multipole expansion*[18]. A general result is that the behaviour of the potential at large distances from the source will be dominated by the first term of the series whose coefficient is not zero[18]. Looking to *multipole* coefficients, the first reads as $K_0 = \int \mathrm{d}v'\rho$, which is the total charge in the distribution. Thus, for equal amounts of positive and negative charge, the system results neutral and the K_0 coefficient is null. In this case, the second coefficient determines the behaviour of the potential at large distances. This latter reads as $K_1 = \int \mathrm{d}v'r'cos\theta\rho$ where r' is the distance of the volume dv' from the centre of the distribution and θ is the angle between r' and the axis passing through the centre and the point in which the potential is being measured. A relevant theoretical result is that for neutral charge distributions, the value of K_1 is independent of the position chosen as origin. The quantities K_0, K_1 are related to what are called *moments* of the charge distribution. Specifically, we call the first *monopole moment*, which is a scalar, and the second a component of the *dipole moment* of the distribution, which is a vector[18]. As the expansion of the *multipole expansion* goes on, more K-coefficients appear, giving more and more details about the problem, however, for our analysis, only the first two have a crucial role, and here I will provide only an analysis of the K_1. Rewriting $r'cos\theta$ as the projection of $\boldsymbol{r}'$ on the direction towards the measurement point, viz $\hat{\boldsymbol{r}}\boldsymbol{r}',$ we can express the contribution of the dipole moment to the potential avoiding the clarification on the origin position, namely:

$$\phi^{K_1} = \frac{\hat{\boldsymbol{r}}}{4\pi\epsilon_0 r^2} \int dv'\boldsymbol{r}'\rho \tag{1.2}$$

From the formula above, we can define the *dipole moment* as:

$$\boldsymbol{p} = \int dv' \boldsymbol{r}' \rho \tag{1.3}$$

which has the dimensions of $charge \times distance$.

A simple but illustrative case is when the charge distribution is built by two single opposites punctiform charges q, situated at a distance d from each other. In this case, the expression for the dipole moment can be easily computed as $\boldsymbol{p} = qd\hat{\boldsymbol{d}}$, where $\hat{\boldsymbol{d}}$ goes from the negative to the positive centre of charge. This case can be used to intuitively understand the behaviour of simple molecules and atoms under the influence of an external electric field.

Assuming that the dipole moments of the molecules or atoms composing a material are in the form of 1.3, we define the electric polarization $\boldsymbol{P}$ as the total dipole moment per unit volume, namely:

$$\boldsymbol{P} = \frac{\sum_i \boldsymbol{p}_i}{V} \tag{1.4}$$

For materials build-up of neutral molecules, only the dipole moments account for the electric field at a large distance. As already stated, whenever an electric field $\boldsymbol{E}$ is applied, the randomly spread dipoles tend to align to its direction, passing from a state of null net polarization to a finite polarization that increases as the external field increases. This process goes on until all the dipoles are coherently aligned to the field, viz when the so-called *saturation point* is reached. For later convenience we define de displacement field $\boldsymbol{D}$ as the effects of an external electric field $\boldsymbol{E}$ and the related total polarization $\boldsymbol{P}$ within a material, namely:

$$\boldsymbol{D} = \epsilon_0 \boldsymbol{E} + \boldsymbol{P} \tag{1.5}$$

This latter, in a more general case, can also be written as:

$$\boldsymbol{D} = \epsilon \boldsymbol{E} = \epsilon_0 \epsilon_r \boldsymbol{E} \tag{1.6}$$

where ϵ, ϵ_r are respectively the absolute and relative permittivity[19].

The nature of the piezoelectric effect is closely related to electric dipoles, above described. Moreover, dipoles near each other tend to align in the so-called *Weiss domains*, which until an external electric field is applied, are collectively randomly oriented[20]. If the applied electric

field is large enough, the process of *poling* happens, i.e. the dipoles orient themselves permanently along the direction of the field. The tendency of a material to change its polarization is called electric coercivity. The higher it is, the higher must be the field to achieve permanent polarization.
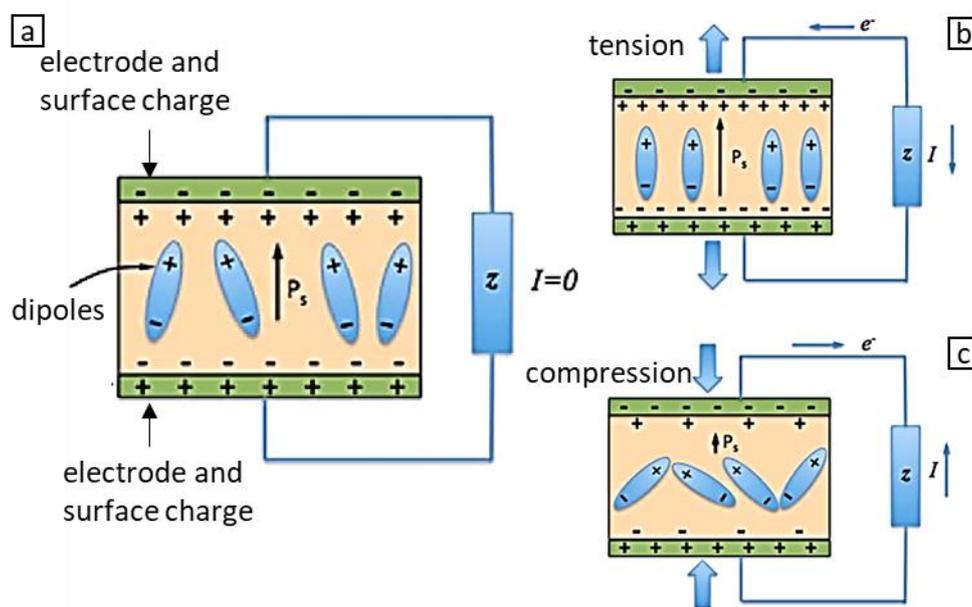
1.1.2 Piezoelectricity

Figure 1.2 Piezoelectric effect across electrical load. a) No mechanical load, b) compressive load leading to a decrease in polarisation relative to the no load condition, c) tensile load leading to an increase in polarisation relative to the no load condition.

Upon all dielectric materials, piezoelectricity arises only from those whom present non-centro-symmetric crystal structures. When an external strain or pressure is applied, the dipoles in the crystals get oriented from a random configuration to a more coherent one. Furthermore, also the vice versa case can arise. Thus, negative and positive free charges appear on opposite faces of the structure, due to the change of polarization. This represents the basic principle of the direct piezoelectric effect and is summarized in Figure 1.2[21]. On the other hand, the application of an external electric field produces the displacements of the charge centres which leads to a

net deformation due to the consequent dipole reorientations. This latter instead, is the basic explanation for the inverse piezoelectric effect.

At low electric fields and low mechanical stresses, the behaviour of the material can be considered in meaningful approximation as linear. Starting from this, the piezoelectric effect reads as the combination of the displacement field D from 1.6 and the Hook's law. In tensorial notation, this reads as:

$$S_i = s_{ij}^E T_j + d_{mi} E_m \tag{1.7}$$

$$D_m = d_{mi} T_i + \epsilon_{ik}^T E_k \tag{1.8}$$

Here, s is the compliance, T the stress S the strain, ϵ the absolute dielectric permittivity and d the matrix of piezoelectric constants. Indexes $i, j = 1, 2, 3, 4, 5, 6$ and $m, k = 1, 2, 3$. These follow the common practice, exposed in Figure 1.3[22], in which $1, 2, 3$ indicate x, y, z and $4, 5, 6$ the shear planes perpendicular to the respective axis[22]. Meanwhile, the superscripts T and E highlight that the electric and stress fields are constant across the system.
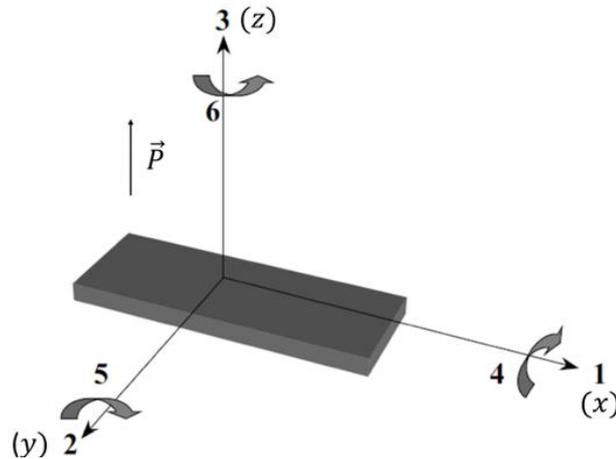

Figure 1.3: Tensor directions defining the constitutive equations 1.7,8.

Varying the indexes, a total of four tensors of piezoelectric coefficients can be obtained. For our investigation, we focus only on the tensor of piezoelectric strain constants d_{ij} which reads as:

$$d_{ij} = \left(\frac{\partial D_i}{\partial T_j}\right)^E = \left(\frac{\partial S_j}{\partial E_i}\right)^T \tag{1.6}$$

The subscripts *i, j* indicate that the electric field applied, or the collected charge, are in the direction of *i* for a displacement, or a force, in the direction of *j*.

Thus, we can mathematically describe the response of the piezo-material to an eternal electric, or force, field. For the sake of this work, our attention is on the component d_{33} of the piezoelectric strain constants tensor, which represents the strain in the direction of the *z*-axis for an electric field applied in the direction of the *z*-axis, too.

1.2 Piezo-materials

In the last few years many active materials such as shape memory alloys and optical fibres, called nowadays with the popular name of *smart materials,* have been developed and patented. Among these, stand the piezoelectric materials. These can be divided into two main subsets, ceramics (also including single crystals) and polymers (together with biological compounds). The former, historically represent the first set of materials presenting piezoelectric proprieties. Example of these are quartz, topaz and lead titanate ($PbTiO_3$). Nevertheless, in their more up-to-date version, piezoelectric ceramics are represented by nanostructures made by inorganic compounds such as ZnO and Zinc Tin Oxids. Piezo-polymers instead, were developed and well-characterized only in the last fifty years, starting from the works of Kawai H. in the early '70[23]. Examples of piezo polymers are *PVDF*, polyamines and polyureas.

1.2.1 Piezo polymers: *PVDF* and P(VDF-TrFE)

Piezoelectric polymers are nowadays deeply investigated, with a few thousand papers produced per year[24]. Their proprieties are so different in comparison to inorganics that they are uniquely qualified to fill niche areas where single crystals and ceramics are incapable of performing as effectively[25]. Even if polymers have a lower piezoelectric strain constant than crystals, they present much higher piezoelectric stress constants; thus, they are much better sensors than

ceramics. Moreover, they offer the advantage of processing flexibility, being lightweight and manufactured into large sheets cuttable in any complex shape. The structural requirements that a polymer should meet to be piezoelectric are: (a) the presence of permanent dielectric dipoles in its structure, (b) the ability to align the dipoles under the influence of an external electric field and to maintain this polarization once it's achieved, (c) the ability to undergo large strains when stressed mechanically[25]. Among the piezoelectric polymers, the semi-crystalline ones play a major role. These, in order to be piezoelectric, must have a polar crystalline phase, whose degree depends on their method of preparation, dispersed within amorphous regions as shown in Figure 1.4[25]. In these materials the piezoelectricity arises from alignments of the crystals in consequence of an external stretch; while the inverse

piezoelectric effect arises from the alignment of the crystal phase in the film plane under the influence of an external electric field.
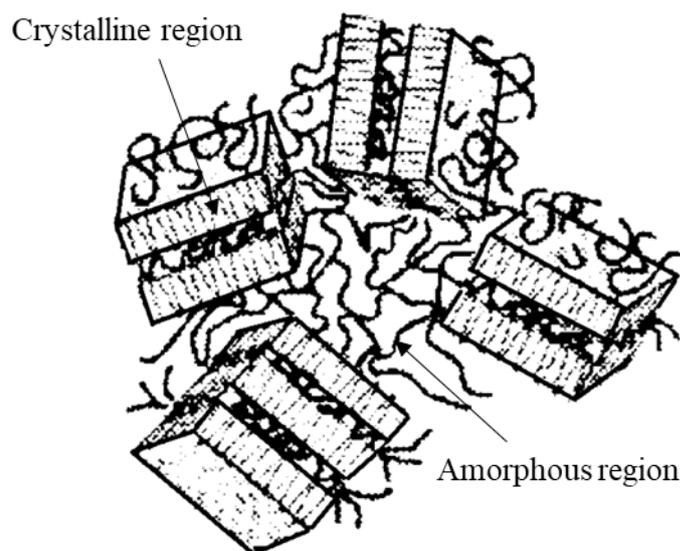
Figure 1.4: Semi-crystalline polymer. Representation of crystal and amorphous regions inside a film plane.

Since the works of Kawai H., polyvinylidene fluoride (*PVDF*) has been one of the most investigated piezoelectric polymers. Detailed descriptions of its most important proprieties have been described in various reports[26,27,28], but among all, what makes it so attractive are its piezoelectric, pyroelectric and ferroelectric proprieties due to its spatially symmetrical-disposed

hydrogen atoms. Moreover, its amorphous phase has a glass transition of $-35°C$: far below room temperature; this makes it flexible for most of its applications. Furthermore, it has a dielectric constant about four times greater than most of the other piezo-polymers. After poling, it has excellent polarization stability which however decreases reaching Curie's temperatures. In addition, *PVDF* is at least made up by 50 to 60% crystal phase and has at least four crystal phases ($α, β, γ , and δ$), three of which are polar.

On the other hand, another piezo-polymer which in the last years has gained the attention of the scientific community is a copolymer of *PVDF*, namely the poly(vinylidene fluoride-trifluoro-ethylene) (*P(VDF-TrFE)*). Because of its predominantly crystallization in the β phase, it presents strong piezoelectric features, together with pyroelectric and ferroelectric ones. Its structure is basically the same as the *PVDF* with the further insertion of *PTrFE*. Compared to its homopolymer, *PVDF-TrFE* presents a much larger crystal phase, up to 90%, thus it exhibits stronger piezoelectric effect and has a higher remnant polarization. Moreover, in the form of single-crystalline film, its d_{33} has reached, in later studies, values of about $-38pm/V$[29], which represents the highest value among synthetic piezo-polymers.

Because of their nice piezoelectric proprieties and their relative low cost of production, *PVDF* and P(VDF-TrFE) both represent the current state of the art in the field of semi-crystalline piezo-polymers.

1.2.2 Piezo-ceramics: *ZnO* and ZTO

In addition to piezo polymers, in recent years materials made up by semiconductive oxides have also gained the attention of the scientific community[30]. *ZnO* nanostructures have been intensely investigated because of their flexibility in numerous applications. Indeed, they carry the advantages of semiconductive materials together with the piezoelectric proprieties of ZnO^2 which originate within its atoms and is repeated throughout the solid due to its high crystallinity[6]. Moreover, depending on the doping, *ZnO* has also a wide-bandgap semiconductivity, high transparency, high conductivity room temperature ferromagnetism and chemical sensing effects[30]. Also, it can be easily integrated with flexible substrates and because of its low cost of production, together with its non-toxicity, it's a good candidate for the technologies of the future. Unfortunately, applications have been restricted by the low electric power output achieved

with the *ZnO* nanostructures[31]. For instance, because of a high free carrier density, a piezoelectric potential screening effect is induced, preventing the manufacturing of stable and large power performances. However further investigations have found that improvements of the power generating of the *ZnO* nanostructures can be achieved controlling the defect and free charge carries throughout thermal annealing treatment, doping and hybridization with polymers[32].

On the other hand, it has been a recent trend to move from single to multicomponent oxides. The multicomponent Zinc Tin Oxide $ZnSnO_3$ presents numerous exploitable proprieties. For instance, both zinc and tin are abundant and recyclable, but also, being a ternary oxide, its proprieties can be tuned adjusting the cationic ratio. Moreover, different shapes can be achieved depending on the production process, and in addition $ZnSnO_3$ also crystallizes in both rhombohedral and orthorhombic structures[33]. $ZnSnO_3$ structures such as nanocubes, microbelts and nanoplates have been shown to manifest piezoelectric and piezoresistive effects, this qualifies $ZnSnO_3$ as a potential material for future energy harvesting devices[34,35]. $ZnSnO_3$ structures that were used for this work were nanowires produced by hydrothermal precipitation in a conventional oven. Although, to verify the efficiency of their proprieties as piezo-materials, a characterization of their d_{33} value must to be done. This will be the aim of the Chapter 3.

1.2.3 Major applications.

As stated, piezoelectric materials can be employed in many applications. One of the applications on which research is focusing the most, is that of energy harvesting structures, i.e. those nanostructures capable of producing energy from small mechanical stresses. Indeed, devices such as pacemakers could be self-powered, if able to extract their own energy from the numerous potential energy sources of the human body, such as the mechanical energy of the muscular movements or blood pressure, or the vibrational energy in the form of acoustic. One of the most promising materials are non-centrosymmetric oxides, which have been taken into account in the last few years because of their spontaneous polarization proprieties, i.e. the starting point for technologies that rely on piezoelectricity. Therefore, *ZnO* and $ZnSnO_3$ nanostructures have been broadly investigated. From these materials, potentials within a large range of frequency

can be generated, leading to applications to devices of many fields, such as self-power generating systems for medical issues, wearables, sensor, actuators and wireless technologies.
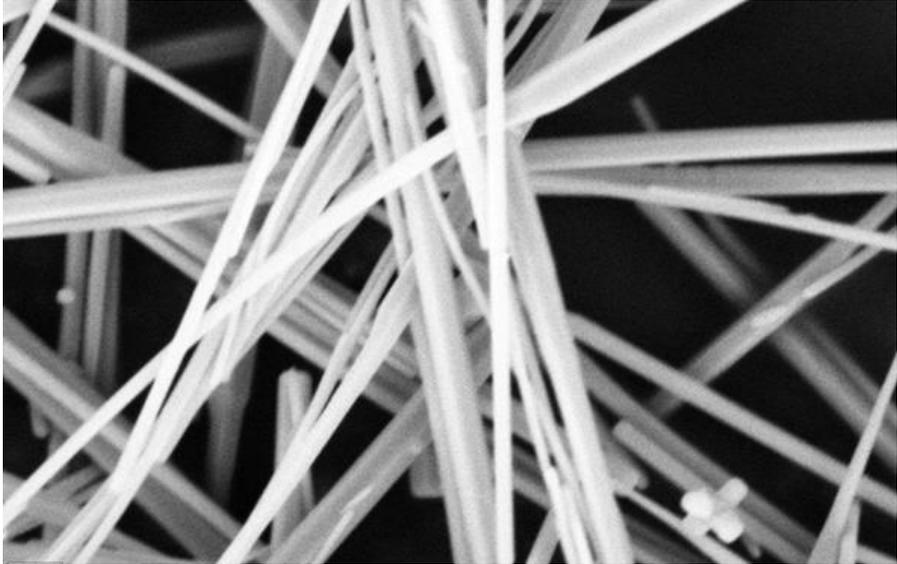

Figure 1.5: SEM image of ZnO nanowires.

One of the most exploited nanostructures for these aims are nanowires. These nanostructures are defined as structures that have a thickness constrained to tens of nanometres and an unconstrained length. Because of these scales, they can be considered as one-dimensional materials. In addition, due to the laterally quantum confinement of the electrons in nanowires, these manifest proprieties that have not been observed in three-dimensional materials. An example of nanowires is provided in Figure 1.5[36].
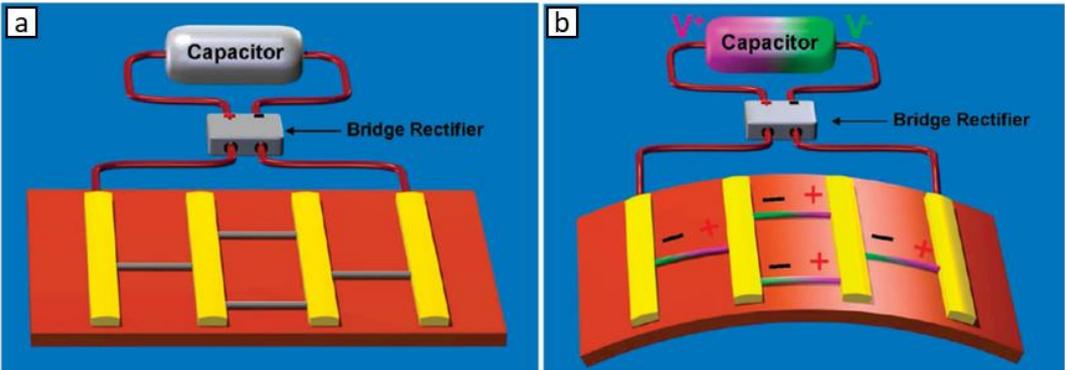

Figure 1.6: Working principle of a flexible substrate-base nanogenerator. a) Schematic diagram of the structure without mechanical deformation, b) Demonstration of the output scaling-up when mechanical deformation is induced.

One of these structures can act like a diode when subjected to mechanical stress, by running the charges to an external circuit under favourable conditions. Moreover, it conducts in one direction only, being ZnO and $ZnSnO_3$ both semiconductors[37]. So, the integration of many coherently oriented nanowires could lead to an enough power supply for such devices. Possible nanogenerators made up by nanowires are for instance: fibres-based[38], hard substrate-based[39], flexible substrate-based[40] as shown in Figure 1.6[4].

Although, many other materials apart from ZnO and $ZnSnO_3$ also manifest strong piezoelectric proprieties that can be exploited for energy harvesting, thus, in order to evaluate their effectiveness analysis on their d_{33}, must be done. The value for the ZnO has been already well documented in literature[41], nevertheless a further value assessment will be done in Chapter 3, in order to use it as a reference for the value of $ZnSnO_3$ which instead hasn't yet a quantitative characterization.

2 Chapter 2 – Instrumental Set Up and Techniques

Atomic Force Microscopy (AFM) is a method used to determine the three-dimensional shape of a surface with sub nanometre resolution. The surface morphology is not investigated in the usual way, i.e. by reflections or shadows. Rather, each point within the provided 2D array represents a measurement of surface height, made using a sharp solid force probe. The basic functioning of the AFM is simple Its basic set up is shown in Figure 2.1[42]. A cantilever with a very sharp tip slides over the surface of the sample. Different operation modes, that will be later explored in their details, can be selected. As the tip approaches, it interacts with the surface throughout various forces, for example Van der Waals or electrostatic forces. Due to the impact of such forces, the tip cantilever is deflected. Cantilever deflection is measured by an SLD beam that is centred at on the cantilever and reflected into a position-sensitive photodiode (PSPD). In typical operation modes a feedback-loop-height control maintains the tip-cantilever interactions at constant setpoint by moving up or downwards the tip-cantilever system. Tracking the changes in cantilever height allows at the end to reconstruct the three-dimensional representation of the surface.
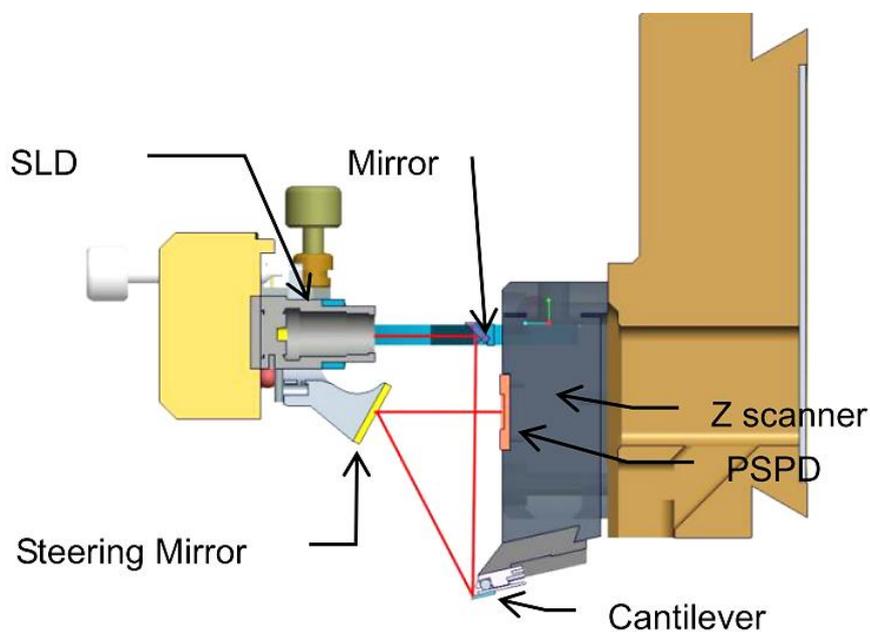

Figure 2.1: basic set up of a Scanning Probe Microscopy

By introducing modulation techniques, atomic force microscopy enables to distinguish the different forces acting on the cantilever and many other measurements can be performed beside the simple morphology. Thus, Atomic Force Microscopy results as a versatile microscopy technology to study samples at nanoscales. In my work, I used NX10 Scanning Probe Microscope of the Park System Corp.

2.1 Techniques

2.1.1 Contact-Mode

Operating in contact mode implies that the tip makes a soft physical contact with the surface of the sample. The system made up by the tip attached to the cantilever has a spring constant lower than the one of the atoms of the sample. Because of this, as the tip touches the surface, the interaction force is more likely to deflect the cantilever, rather than deform the sample. However, when the cantilever reaches its maximum deflection, a deformation of the sample can happen. So, the cantilever gently traces the sample bending under the effect of the contact forces. A more detailed analysis of the physical scenario is done by taking into account the Van der Waals forces[42]. As the tip approaches the surface, their atoms get first weakly attracted. This interaction goes on until the reciprocal distance is so little that their electronic clouds start to repel each other due to electrostatic forces. Therefore, further decrease in the distance leads to the weakness of the attractive component of the Van der Waals forces, that goes to zero when atoms are at apart about the length of an atomic bond. Then, when the Van der Waals forces become positive, i.e. repulsive, the atoms are in contacts. Because of the steepness of the Van der Waals force in the repulsive region, any force that attempts to push the atoms closer gets almost entirely balanced. Therefore, any attempt of the cantilever to penetrate the surface of the sample is instead turned into deflections. So, increasing the force is more likely to cause the deformation of the surface, rather than a closer contact. A basic representation of the Van der Waal forces is provided in figure 2.2[43].
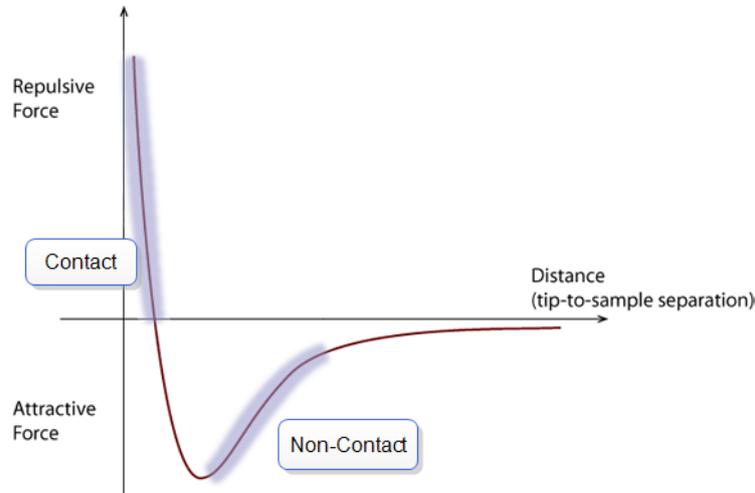
Figure 2.2: Van der Waal's force vs distance, based on the Lennard-Jones model.

The position of the cantilever is tracked with optical techniques. As stated, the movements are collected as the movements of an SLD light beam centred on the cantilever by a PSPD. This latter can measure displacements of light in the order of $10\text{Å}m$; furthermore, because of the ration of the path length between it and the cantilever and the length of the cantilever itself, the system can detect sub-angstrom movements, due to the resultant mechanical amplification. Once the deflection is detected, it is used as an input to a feedback-loop circuit. Consequently, the z-servo is moved in order to restore the SLD beam on its setpoint on the PSPD; thus, the force between the tip and the sample is maintained constant. The resulting image is so generated from the motion of the z-scanner. Trough this technique, be can measure simultaneously topography and other characteristic, such as friction forces, spreading resistance and piezoelectric proprieties. However, Contact-Mode presents several disadvantages. For instance, soft samples can be destroyed by the tip and also this latter is consumed by the rubbing. Moreover, speed scanning must take into account the feedback-loop and its response time, ; thus, leading to longer acquisition times compared to other modalities[44].

2.1.2 Non-Contact Mode

Relying on the spatial shape of the Van der Waals forces allows further methods of investigation. In Non-Contact AFM the cantilever does not touch the surface of the sample, instead, it

vibrates at its resonant frequency over it. In this operation mode, the space between the two structures is about $1-10\text{Å}$. In contrast with Contact Mode, which relies on repulsive forces, the Non-Contact Mode measures topography throughout the attractive ones. Consequently, the force between the tip and the sample is very low; thus, a direct measurement of its variation is very difficult to achieve. In NCM, one detects the slight changes that the attractive surface forces induce to the vibration phase or the vibration amplitude of the cantilever.
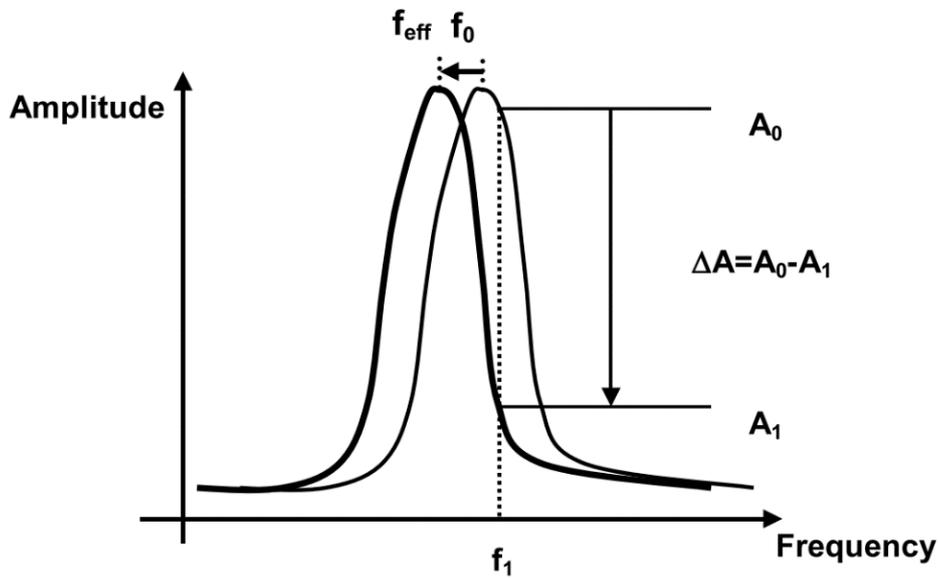
Figure 2.3: oscillation amplitude vs frequency in a neighbourhood of the resonance frequency

The first step is to determine and fix a value for the resonance frequency f_0 of the cantilever. This is done by driving the cantilever vibration with a bimorph at a fixed amplitude and varying the frequency until the resonance phenomenon occurs. Then, it has to be considered that, as the tip vibrates, its interaction with the surface changes its intrinsic spring constant k_0. As the system tip-sample-force can be modelled as a forced harmonic oscillator and the resulting effective value for the spring constant k_{eff} is defined through the following relation:

$$k_{eff} = k_0 - \frac{\partial F(z)}{\partial z} \tag{1.1}$$

As the value k_{eff} changes, also does the value of the resonance frequency, leading to a new value f_{eff}. Indeed, the following relation holds:

$$f_{eff} = \sqrt{\frac{k_{eff}}{m}} \tag{1.2}$$

where *m* is the mass of the cantilever. As shown in Figure 2.3[42], vibrating the cantilever at a frequency f_1, for instance, a little larger than f_0, a little shift to f_{eff} leads to a large change in amplitude. This large change is due to the steepness of the frequency vs amplitude graph in a neighbourhood of the resonance frequency. Therefore, is possible to relate the amplitude change ΔA measured in f_1 to the height change Δd, namely the distance between the probe and the surface. Then, as the change in amplitude is measured, a feedback loop compensates the resulting change in distance using the *z*-stage. The topography image is build maintaining constant the amplitude A_0 and the distance d_0. Moreover, the difference between the amplitude oscillation and its set point, is what we refer as *Non-Contact Mode Error Signal* (*NCM Error Signal*)

2.1.3 Electrostatic Force Microscopy (EFM)

In most investigations, the simple topography image is not enough to well characterize a material. For instance, topography doesn't contain information about the electric or piezoelectric proprieties. Nevertheless, various techniques perform this task. The Non-Contact EFM is one of these. Proprieties such as the surface potential and the charge distribution are obtained by applying a bias to the tip and measuring the deflections of the cantilever under the electrostatic forces that arise. The most refined EFM technique is the so-called *enhanced* one which relies on a lock-in amplifier[42]. This latter fulfils two tasks: on one hand, it applies to the tip an AC bias of a frequency ω, whereas on the other it separates this latter frequency to the output signal. Indeed, the signal obtained by the enhanced EFM consists in both surface topography and electrical proprieties generated by the Van der Waals and electrostatic forces respectively, and the key of the effectiveness relies on the ability to separate these signals. Taking into account also the possibility to apply a DC bias to the sample base, the overall expression for the electromagnetic potential that arises in the system is given by:

$$V(t) = V_{DC} - V_s + V_{AC}sin\omega t \tag{2.3}$$

where V_{DC} is the potential to the sample base, V_s is the native surface potential of the scanned area, and V_{AC} and ω are respectively the amplitude and the frequency of the external AC voltage. Modelling the system as a parallel plate capacitor model, the equation for the dynamic, taking into account also equation 2.3, reads as:

$$F(t) = \frac{C \times V^2}{d} = \tag{2.4}$$

$$= \frac{C}{d}\left\{(V_{DC} - V_S)^2 + 2(V_{DC} - V_S)V_{AC}sin\omega t + \frac{1}{2}V_{AC}^2(1 - cos2\omega t)\right\} \tag{2.5}$$

Here F is the electrostatic force acting on the tip and C the capacitance of the system. Starting from Equation 2.4, the signal can be analysed in terms of its three separate parts. Indeed, DC deflection can be read directly from the software and the AC signals can be read by the lock-in system, which can read either the part with a frequency of ω or 2ω. These latter, contain respectively information about the surface charge and the surface capacitance gradient (viz dC/dz). In conclusion, applying an AC bias with a frequency ω to a tip oscillating with a frequency f over a surface, two interactions arise: the electrostatic one and the Van der Waal's one. From this, using precise and different values for the frequencies ω and f is possible to extract both information about topography and electrostatic proprieties. Usually the frequency ω of the AC bias is of $17kHz$; whereas f is chosen accordingly to the cantilever proprieties.

2.1.4 Piezoelectric Force Microscopy (PFM)

Piezoelectric Force Microscopy investigates the electromechanical proprieties of a material. In this technique, a conductive tip is in contact with the surface of the sample and an AC bias is also applied. The AC bias has a frequency ω of $17kHz$ as for the EFM. Because of the bias, an electric field arises between the two surfaces. Therefore, if the investigated material is piezoelectric, its surface will start to oscillate because of the inverse piezoelectric effect. Instead, oscillations due to varying electrostatic forces from Equation 2.5 are suppressed due to strong contact forces. This is fundamental in order to acquire high-quality PFM data. From the theory

of Chapter 1, we know that the strain S_j developed in a piezoelectric material is proportional to the applied external electric field E_i by the piezoelectric coefficient d_{ij}. This relation reads as:

$$S_j = d_{ij}E_i$$

(2.6)

where the indices follow the convention of Figure 1.3. Assuming that the strain and the field in the longitudinal direction are expressed as:

$$S_3 = \Delta z/z_0$$

(2.7)

$$E_3 = V/z_0$$

(2.8)

where z_0 is the thickness of the sample, the so-called longitudinal piezoelectric constant, viz d_{33}, can be determined by measuring the z-displacement along the field applied in the z-direction, namely:

$$\Delta z = d_{33}V$$

(2.9)

If the initial polarization of the investigated Weiss domains is perpendicular to the sample surface and parallel to the field, the displacement will be positive. Instead, if the polarization is antiparallel, the displacement will be negative. Under the influence of the AC bias, the displacement of the surface reads as:

$$\Delta z = d_{33}V_{AC}cos(\omega t + \varphi)$$

(2.10)

where φ is the difference in phase between the applied voltage and the acquired signal. This latter phenomenon is due to the coupling of the AC field with the internal electric field caused by induced orientation of the dipoles. For instance, if the field and the bias are parallel $\varphi = 0$; instead, if they are anti-parallel $\varphi = \pi$. This oscillation is then filtered by the lock-in amplifier and used to determine the polarization direction of the sample together with the magnitude of the displacement. Thus, PFM amplitude together with PFM phase are acquired[42]. To avoid the permanent switching of the domains, a bias lower than the coercive value is applied. Nevertheless, it has to be said that, for most of the real cases, the studied samples contain randomly oriented polycrystalline structures whose lateral components of the d_{ij} are not null. Thus, the vertical response of the sample to the vertical electric field is no longer proportional to the d_{33}

alone, but also to d_{31} and d_{15}. However, this eventuality will not be taken into account in the present work.

Piezoelectric Force Microscopy can be used both for global and local mapping of the proprieties of the material. In the latter case, also a DC bias to the sample base is usually connected in series with the AC one to the tip. For large enough DC biases is possible to polarize permanently the samples. Alternating ON states, in which the DC bias is applied, to OFF states, in which the DC bias is null, it is possible to measure the local polarization loop for the material. This technique is the so-called Switching Spectroscopy.

For the sake of this work, it must be said that Equation 2.9 refers to the ideal case. Indeed, measurements operated with an instrument must consider also the sensitivity S of this latter. Thus, tanking sensitivity into account, Equation 2.9 reads as:

$$\Delta z = S d_{33} V \qquad (2.10)$$

The sensitivity can be measured in two ways. The first is through the built-in features of the instrument. The second is using a standard sample with a well-documented piezoelectric coefficient. In this thesis I will follow the second path, using P(VDF-TrEE) as my standard reference.

2.2 Cantilever selection

Depending on the technique, several types of cantilevers can be chosen. For instance, in contact mode, is better to choose cantilevers with low spring constants, in order to have a more sensitive response to the differences in level of the surface. Usually, the cantilevers for this technique are also very thin, thus, a lower spring constant can be achieved. When comes to Non-Contact Mode, cantilevers are usually thicker than Contact-Mode, and have a high resonant frequency. Moreover, in order to choose the right cantilever, other parameters such as the coating, and the ratio between the tip radius and the structure that one wants to analyse on the sample. Indeed, the radius of the cantilever should always be lower than the smallest detail of the sample, in order to have the best definition. Furthermore, also the price must be taken in account. Sharper

tips are more expansive than thicker ones, also, the damage more often. For my measurements I used different cantilever. For the *PVDF-TrFE*, a *multi75E*[45] and a *NSC36/Cr-Au*[46]. The first one was used for EFM and Switching Spectroscopy, while the second one was used for the NCM topography and PFM. For the *ZnO* was used the *multi75E*, while for the *ZnSnO$_3$* was used the *NCS36/Cr-Au*.
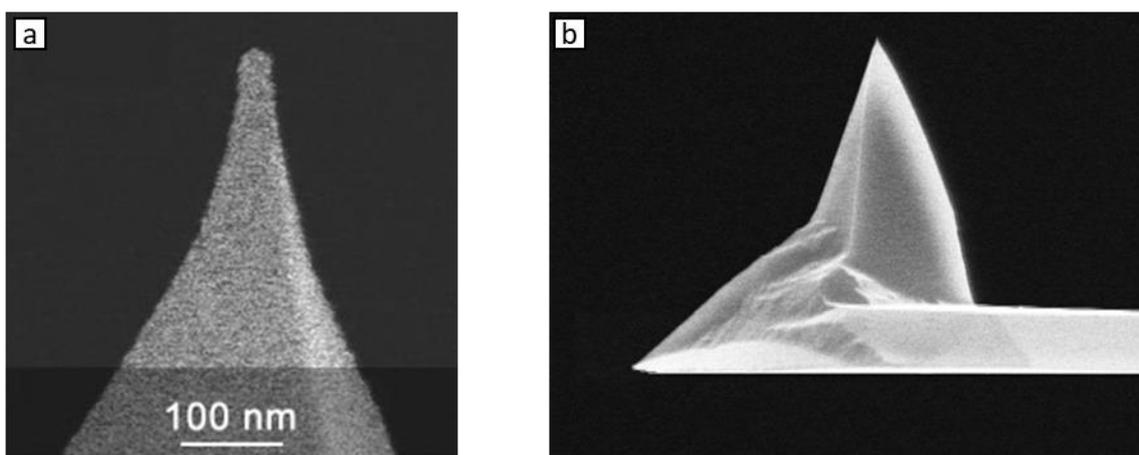

Figure 2.4: two distinct cantilevers, details of their tips. a) NSC36/Cr-Au, b) multi75E.

2.3   Sample Manufacturing

The ZnSnO$_3$ nanowires were produced by the department of Material Science of the University of Lisbon throughout a hydrothermal synthesis in a conventional oven. Once nanowires were synthetized, they were then centrifuged at 6000 rpm and washed several times with deionized water and isopropyl alcohol, alternately. Finally, nanostructures were finally dried at 60 °C, in vacuum, for 2 hours. The chemical details are reported in literature[37,47]. PVDF-TrFE was produced at Max Plank Institute of Mainz using a deposition technique called solution micromolding. Also here, more details are in literature[31,48].

3   Chapter 3 - Samples Analysis and Discussions

In this chapter, I present and discuss the most significant results obtained on the three different samples, respectively the *P(VDF-TrFE)*, the *ZnO* and then the $ZnSnO_3$. The measurements were performed with EFM and PFM techniques with the purpose to quantify the piezoelectric response of the studied materials.

3.1   P(VDF-TrFE)

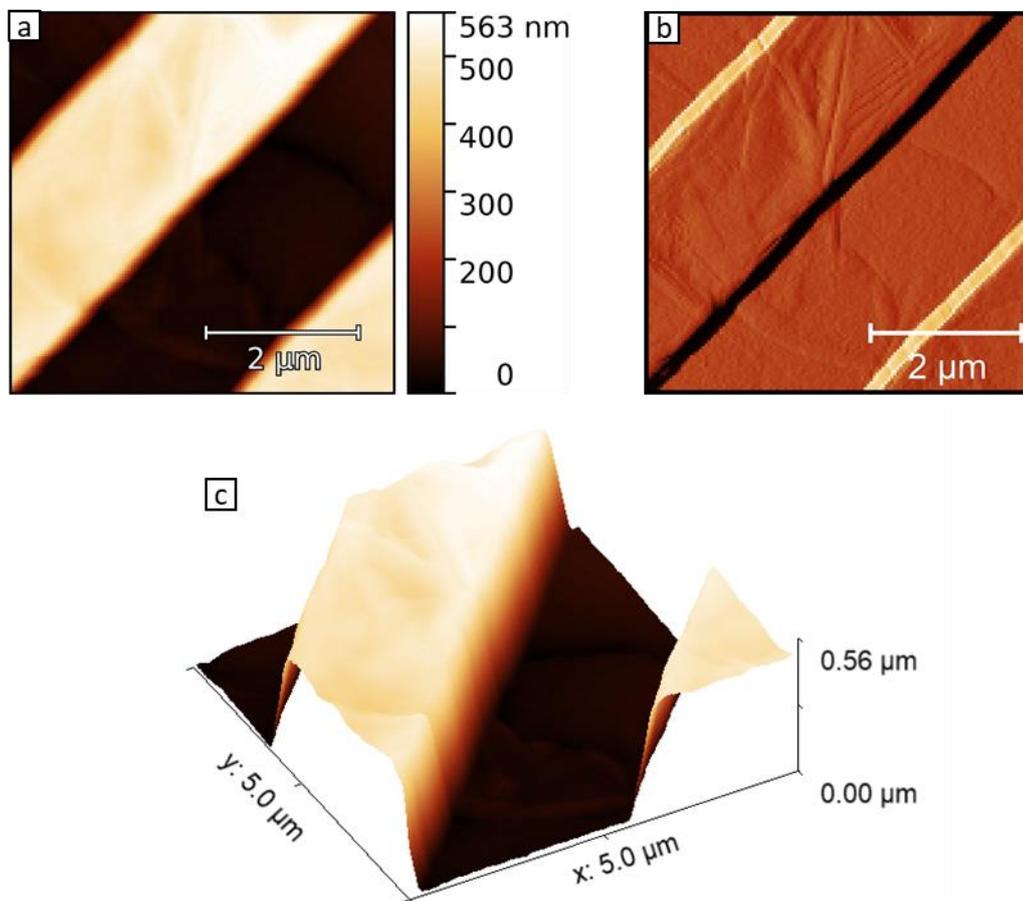*Figure 3.1: Investigation of P(VDF-TrFE) micropatterned thin film by non-contact mode force microscopy a) topography, b) NCM error signal c) three dimensional, not to scale representation of the topography.*

In my initial experiments I used *P(VDF-TrFE)* as a reference piezo-electric thin film material. Indeed, its piezoelectric proprieties have been investigated by different macroscopic and

microscopic measurements and are in detail described in the literature. Here I use the PFM measurements and the known d_{33} value to calibrate the instrument sensitivity.

The first step was to find a suitable area for the studies. Figure 3.1 shows the result of a 256pixels scan of a 5µm × 5µm area of the *P(VDF-TrFE)* sample surface. The choice for the tip was on an *NSC36/Cr-Au*, thus, line scans were performed in Non-Contact mode in order to not damage its Cr-Au coating. In Figure 3.1a we can appreciate the surface of the polymeric sample. The image provides an insight on its repetitive pattern, which goes on along the whole surface. As it is clear from the false-colour legend alongside, the darker areas correspond to wells, whereas the lighter ones correspond to peaks. Both wells and peaks are about 2µm wide. Moreover, the height of the peaks above the wells is around $500 - 600$nm. In Figure 3.1c, a three-dimensional not to scale representation of the scanned area is provided to better appreciate its morphology. In addition, Figure 3.1b shows the NCM error signal acquired during the EFM. The error signal shows more clearly the local contrast in surface topography and crystalline structures appear embedded in the amorphous phase. The few crystallites observed are long and thin with a dimension around hundreds of nanometres long and tens of nanometres thick, with directions randomly oriented.
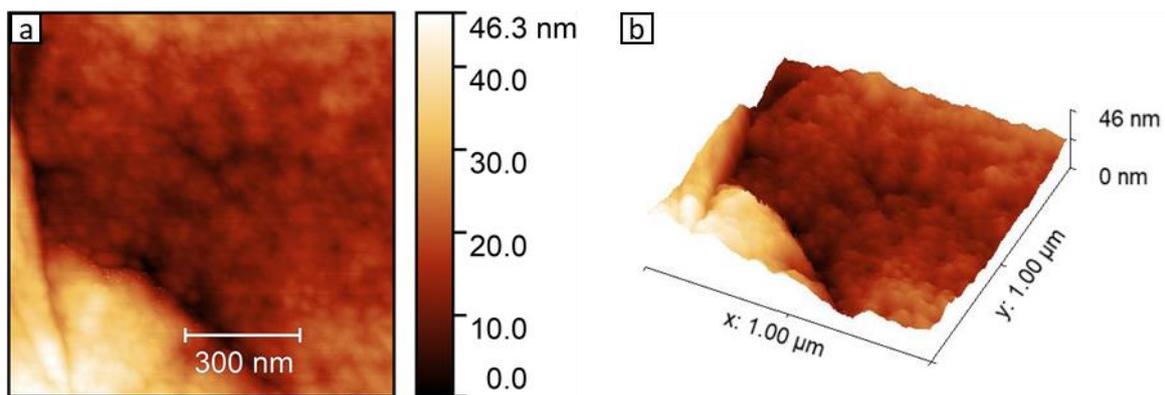

Figure 3.2: P(VDF-TrFE) a) topography and b) three-dimensional not to scale representation of a well area.

Once the morphology of the sample was clear, the next step was to position the probe on a well area and perform a PFM scan. Even though wells and peaks are both piezoelectrically responsive, the choice for the firsts was made because of the thinness of the film. Indeed, a thinner film has also a lower coercive field, thus a polarization switching of piezoelectric domains can be achieved at lower potentials. Figure 3.2a provides an insight on a well surface morphology. The $1\mu m \times 1\mu m$ scan shows that its surface has differences in height of about $50 nm$.
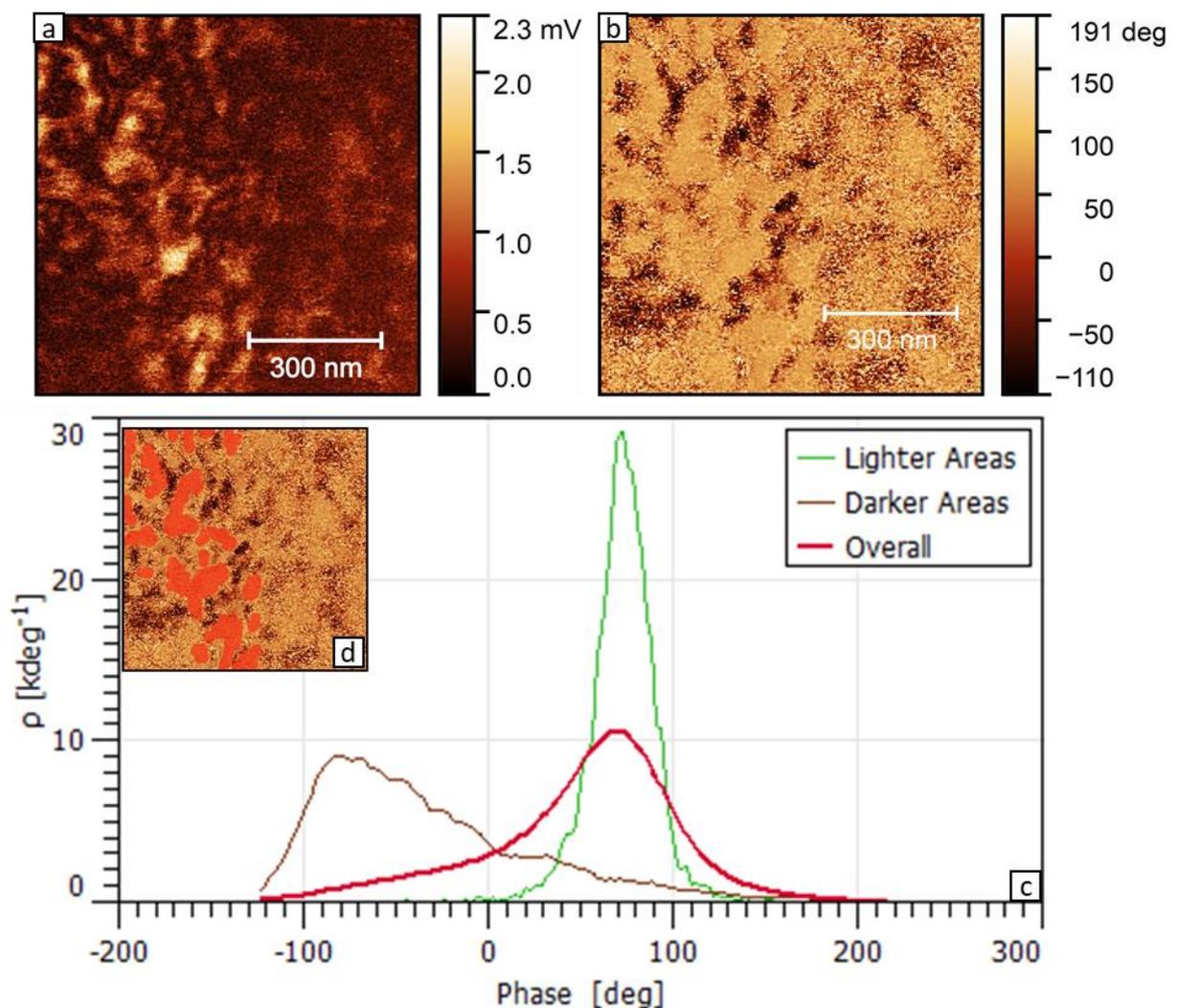

Figure 3.3: PFM on an unpolarized well area of the PVDF-TRFE sample. a) PFM Amplitude, b) PFM Phase response, c) Distribution of phase response, overall and domain to domain view, d) domains referred to as "lighter areas"

This applies for the whole sample, allowing us to state that wells are almost flat surfaces. Figure 3.2b provides a three-dimensional representation of the scanned area, in which the magnitude of the height is not to scale to better appreciate the morphology.

Once above a suitable well, a first set of PFM analysis was performed in order to reveal the piezoelectric properties of the polymer. The first step was to apply a $+3V$ AC bias to the tip and measure the PFM amplitude response of a $1\mu m \times 1\mu m$ area positioned in a well of the sample. The response is plotted with a pictorial representation as explained by the legend alongside. From the image, we can see that some areas behave differently than their neighbourhoods. For instance, the lighter areas, presents larger deformations under the influence of the electric field. An explanation for this phenomenon is that among the crystal phase, some polarization vectors are coherently aligned in Weiss domains. As it is evident, the values are provided in mV, because the data we acquired through the PSPD. A conversion from $volts$ to $meters$ can be done knowing the d_{33} component of the polymer and the applied bias throughout the formula:

$$d_{33}\,[\text{m/V}] = \frac{D_{17kHz}[m]}{V_{17kHz}[V]} \tag{3.1}$$

where $D_{17kHz}[m]$ is the deformation in meters of the sample reacting to $V_{17kHz}[V]$, namely the 17kHz bias.

As stated at the beginning of the chapter, the d_{33} component for *P(VDF-TrFE)* is assumed from literature in order to be used for the extraction of the instrument sensitivity. The PFM phase response of the sample is provided in Figure 3.3b. As we can see, from the analysis arise two types of domains, exposed by different colours. Different areas of the well surface react in different ways to the AC bias depending on the orientation of their corresponding polarization vectors. As we can see, light areas, explicitly evidenced in Figure 3.3d, mainly present a phase response that stands around a small neighbourhood of $+80°$. Meanwhile, the darker areas present a distribution mostly around $-90°$. Indeed, they both represent native polarization domains, or Weiss domains. In Figure 3.3c, we can best appreciate the distribution of the phase of the domains. A large component of phase vectors is around $+90°$; nevertheless, we have a significant component also for the randomly oriented ones.

Once the response to the PFM investigations was detected, a polarization of the sample was performed. This latter consists in applying a bias to the tip or to the sample. If the bias is large

enough, an orientation and alignment of the polarization vectors of the crystals can be achieved. The procedure was performed equipping a *multi75E* tip. The choice of the tip was done in order to better operate in Contac Mode and thus better polarize the sample. The polarization was then performed in EFM by applying ±10VDC to the sample, while keeping the tip at ground potential.
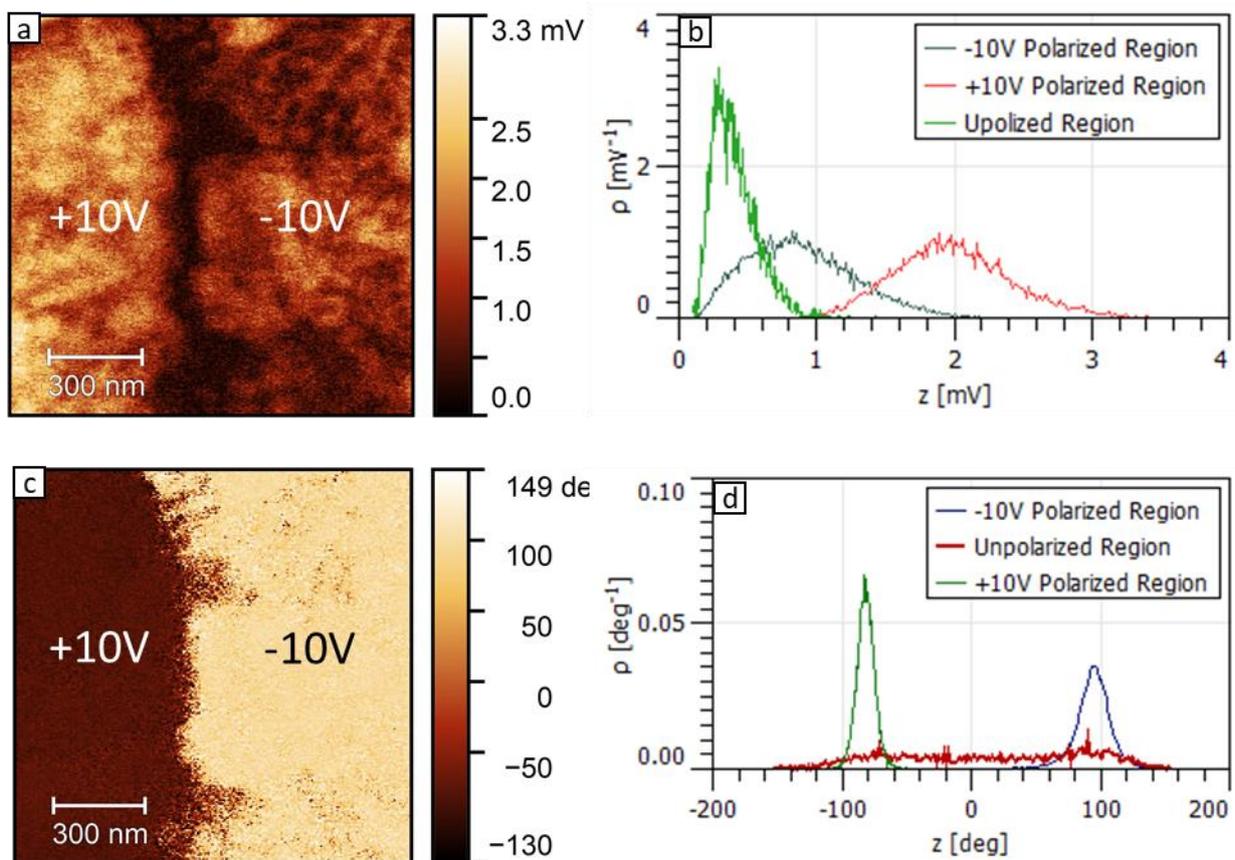
Figure 3.4: PFM on a polarized well area of the PVDF-TRFE sample. a) PFM Amplitude response, b) PFM Amplitude response distribution for differently polarized domains, c) PFM Phase response, b) PFM Phase response distribution for differently polarized polarize.

Figure 3.4 Demonstration of polarization switching in PVDF-TRFE thin film. The area scanned is different from the one of figure 3.3. Before the acquisition of the image, the whole area was polarized with a -10V bias. Then the sole left half of the shown area, was polarized with a +10V.

A 180° change in the EFM phase signal is observed while the EFM amplitude remains of similar magnitude.

The results are shown in Figure 3.4a. The EFM amplitude response is larger in the left half than the right one. This fact is also visible in Figure 3.4b, where the distribution of the EFM amplitude is plotted. Furthermore, in Figure 3.4c we have the PFM phase response of the remnant polarization. As evident, after large enough biases are applied, two clearly defined regions arise. As we can see from Figure 3.4d, the left side reacts around a neighbourhood of −90°, whereas the right side reacts in a neighbourhood of +90°. This latter is strong evidence that the two sides of the sample were fully polarized in two opposite directions due to the two opposite biases applied. Moreover, from Figure 3.4d, we can also appreciate that the PFM phase response of the area is almost uniformly distributed in the -90°, +90° range. Moreover, among the two halves of the scanned area, we see a so-called domain wall. This region is evident both in Figure 3.4a, where it results darker, and in Figure 3.4c, where it results fuzzier. Referring to Figure 3.4b, we appreciate quantitively how less responsive this region is compared to its neighbourhoods. Whereas from Figure 3.4d, we see that the phase of the domain wall is uniformly distributed between −90° and +90°.
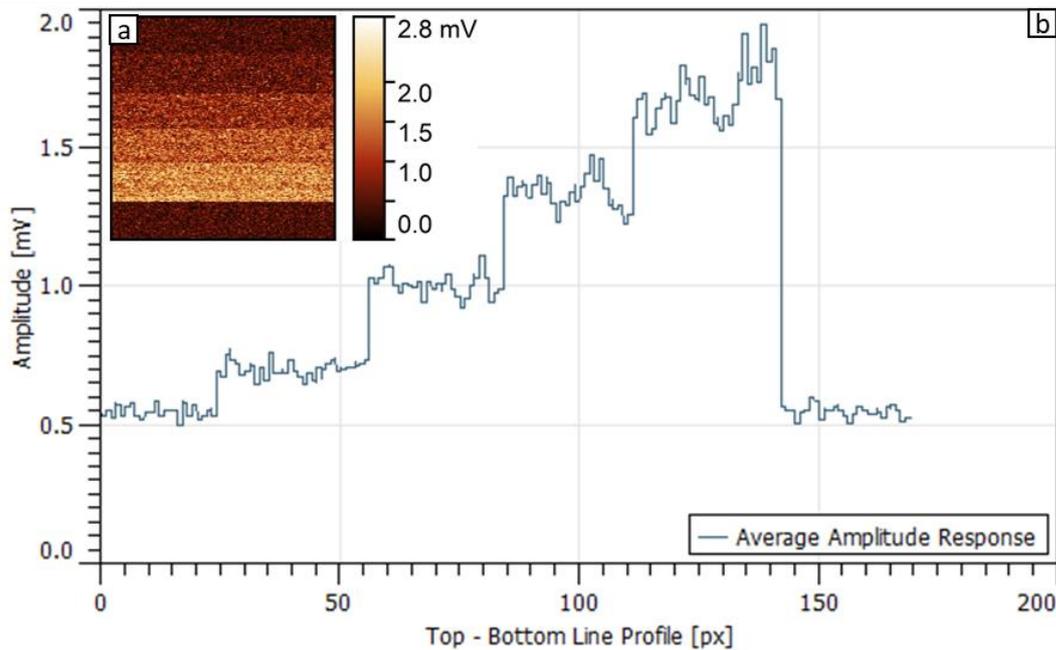
Figure 3.5: PFM on a single well point of P(VDF-TrFE) thin film. a) PFM amplitude response, b) top-bottom horizontally averaged cross section of the PFM amplitude response.

After the piezoelectric responses of *P(VDF-TrFE)* were checked, I proceeded in the determination of the instrument sensitivity based on the known d_{33} value of P(VDF-TrFE). To do so, the AC bias was applied on a single point of a well in order to collect information about the inverse piezoelectric effect. This was the crucial stage of the experiment. A *multi75E* cantilever was used. Figure 3.5 shows the response for the bias values of 0, 1, 2, 3, 4, 0V. The data plotted in Figure 3.5b refer to a top-bottom line section of the values reported in Figure 3.5 averaged on horizontal lines. As evident from the image, as the bias changes, also does the amplitude response. Indeed, to higher voltages correspond larger deformations because of the inverse piezoelectric effect. Also here, the amplitude magnitude of these deformations is provided in mV because, as already stated, the data were collected throughout the PSPD. Furthermore, must to be noted that, because of the background noise, to a $0V$ bias corresponds a non-null PFM amplitude response. The overall behaviour of the *P(VDF-TrFE)* perfectly accords with its already known piezoelectric proprieties.

Recalling Equation 2.10, an estimation of the instrument sensitivity can be written though the notation of this chapter as:

$$S[V/m] = \frac{D^{AC}_{17kHz}[V]}{d_{33}[m/V] \times V^{AC}_{17kHz}[V]} \tag{3.2}$$

where $D^{AC}_{17kHz}[V]$ is the deformation expressed in $Volts$ and V^{AC}_{17kHz} the AC bias applied to the tip.
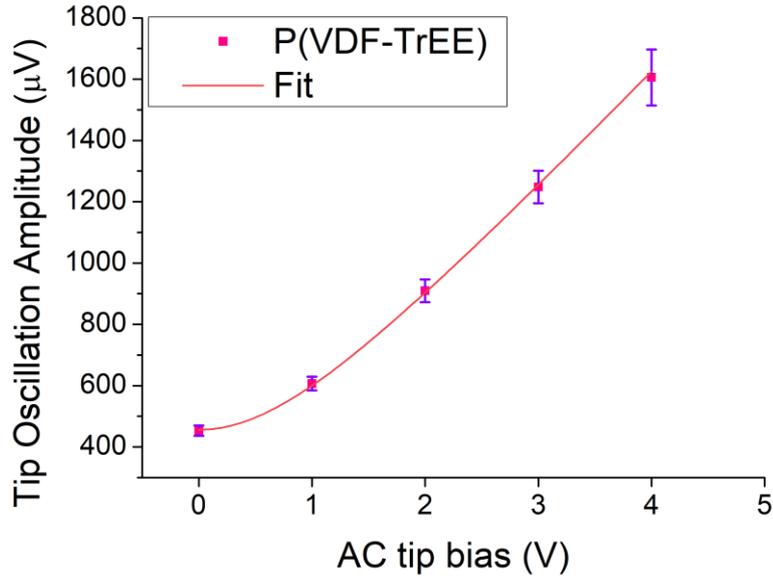
Figure 3.6: P(VDF-TrFE) thin film. Average PFM amplitude response to an AC varying tip bias, data points and their fit.

In Figure 3.6 is plotted the average value of the tip oscillation amplitude for each value of AC bias. Here, errors refer to the standard deviation. From these data we can extrapolate an estimation of the sensitivity S throughout the fit with the function:

$$D^{\alpha}_{17kHz}[V] = \sqrt{N + (d_{33}[m/V] \times V^{AC}_{17kHz}[V] \times S[V/m])^2} \tag{3.3}$$

In quation above, $D^{\alpha}_{17kHz}[V]$ is the tip oscillation amplitude which also takes the background noise N into account. This latter and the sensitivity S are the fitting parameters. Here, value for the d_{33} is fixed to the standard value for the PVDF-TrFE, namely $-38pm/V$. In conclusion, trhoughout this procedure, the value obtained fo the sensitivity was $S = 10.4 \pm 0.1 V/\mu m$. It

has to be said that for the sake of precision a calcoulation of the sensitivity should be done also for the NSC36/Cr-Au tip. However in this work I will not do it.

Figure 3.7: Switching Spectroscopy on P(VDF-TrFE) thin film. a) typical hysteresis of polarization, b) typical butterfly loop of the piezoresponse.

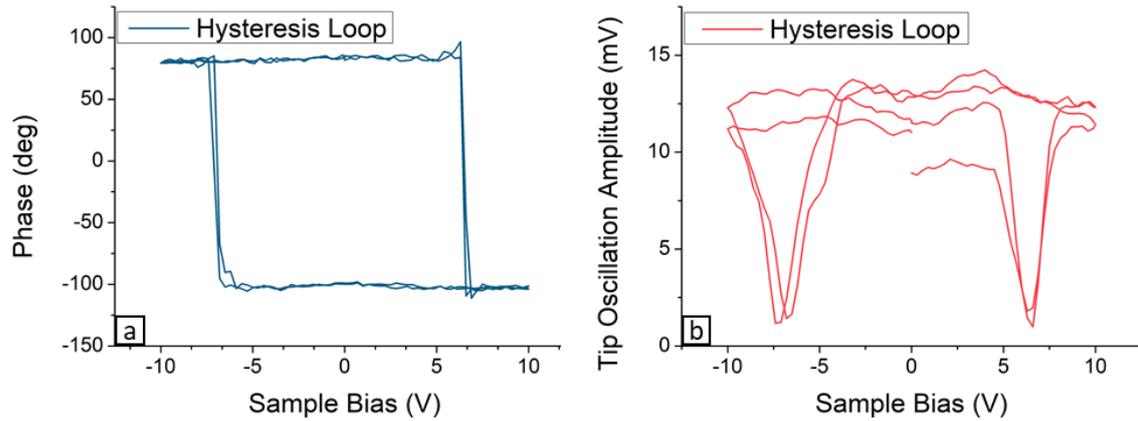Once the sensitivity was calculated, Switching Spectroscopy was performed to demonstrate reversible polarization switching. An NSC36/Cr-Au tip was used and data were collected during two duty cycles, each of $70s$. The DC sample voltage went from $-10V$ to $+10V$, whereas to the tip was applied an AC bias of $3V$. Figure 3.7 shows -in both images- the typical features of the piezoelectric behaviour. In Figure 3.7a is presented the hysteresis loop of the phase response of the single point taken in account. Starting from a value of $0V$ bias, we appreciate that up to about $6V$ the phase remains stable around $90°$, while above $7V$ it drastically drops at about $-100°$, symptom that the bias has reached its coercivity value. The same happens whenever the potential reaches a value of about $-7V$. Here the phase response reaches again $+90°$, symptom that a new coercivity value has been reached. The image also shows that as the external bias reverses its modulus the phase does a $180°$ change in its value, thus an estimation for the coercive potential of about $15V$ can be made. Besides, Figure 3.7b shows the characteristic "butterfly" loop of the amplitude response to the Switching Spectroscopy analysis. Here, as the bias reaches the coercivity value, the amplitude response drops to zero. An intuition to this phenomenon is that, for biases near and near the coercivity value, the amplitude gets larger and

larger, but because the increasing disorder of the system, which is still not enough stimulated to orient in coherent directions, the overall resulting oscillation is minimal. These observations complete the observation on the switching behaviour of the *P(VDF-TrFE)*.

3.2 ZnO
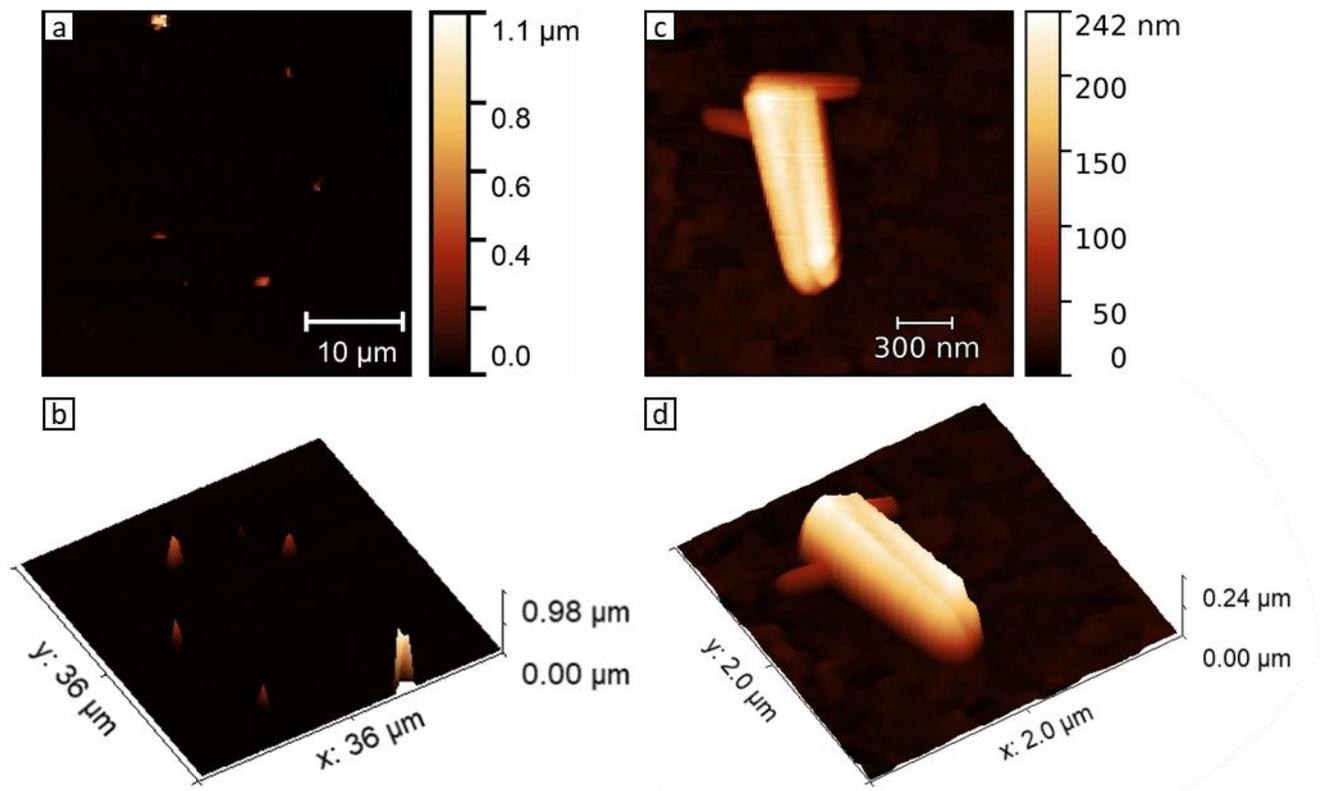
Figure 3.8: investigations of ZnO by non-contact mode force microscopy. a, b) To-pography and not to scale three-dimensional representation of the sample surface; c, d) topography and not to scale three-dimensional representation of a ZnO crystal.

As the sensitivity was extracted from the *P(VDF-TrFE)* analysis, we were able to proceed with the measurements on *ZnO*. Figure 3.8a shows a $36\mu m \times 36\mu m$ scan of the surface where the *ZnO* crystals were deposited. A three-dimensional not to scale representation is also provided in Figure 3.8b. These images were the starting point for the determination of the structures to analyse. All investigations were done implementing a $multi75E$ tip in Non-Contact in order to avoid crystals shifting and damage from the tip dragging. Figure 3.8c shows the selected

structure for the following PFM investigations. As evident from the three-dimensional not to scale representation in Figure 3.8d, the structure appears solid with sharped and nicely defined edges. This leads us to speculate it being an actual well grown crystal.
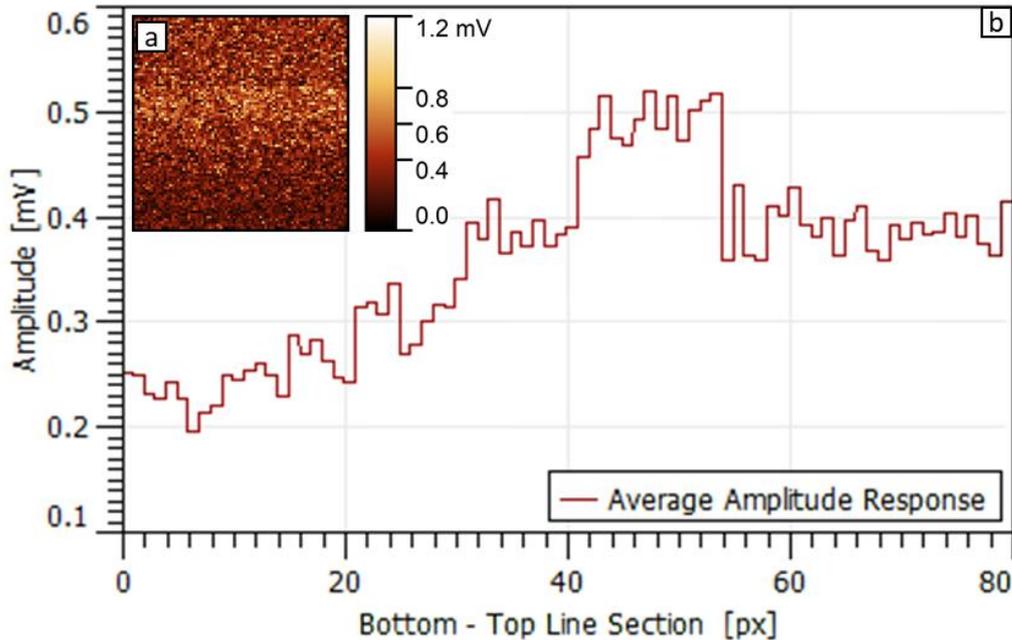
Figure 3.9: a) PFM Amplitude response to a varying bias of a single point of the ZnO crystal, b) bottom-top horizontally averaged PFM Amplitude response.

Once the crystal was selected, the probe was landed on a single point of its surface in order to proceed with the PFM investigation. As was done for the *P(VDF-TrFE)*, an AC bias was applied to the tip for the values 0, 1, 2, 3, 4, 0V. Each pixel of Figure 3.9a) represents a data point which together encapsulate the results of this procedure. The response of the sample surface to stimuli is plotted in Figure 3.9b. Here is presented a bottom-top cross-section of the values reported in Figure 3.9a averaged on horizontal lines. As for the *P(VDF-TrFE)*, an increasing bias leads to an increasing PFM amplitude response. This is a strong evidence of the piezoelectric proprieties of the *ZnO* crystal. Also here, must to be noted the non-null value of the PFM amplitude for a null bias applied. This again, founds its roots in the background noise registered by the tip.
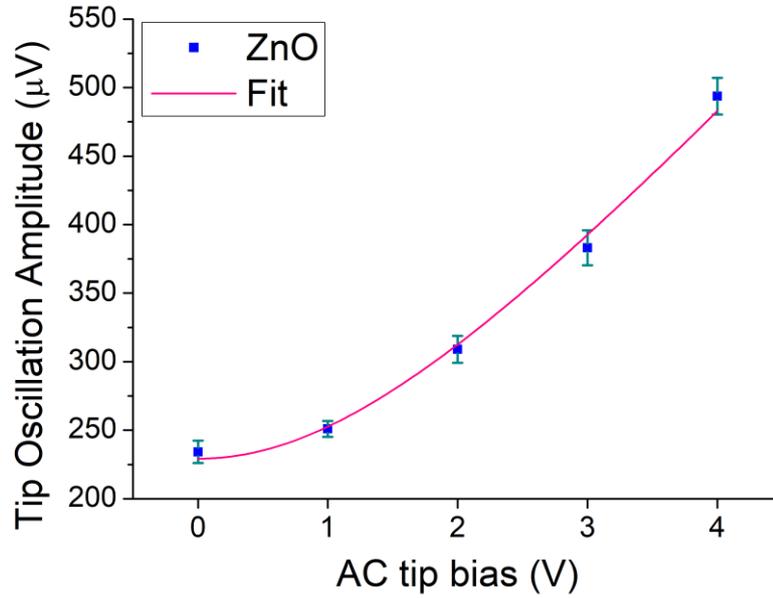
Figure 3.10: PFM response of a ZnO nanocrystal. Average PFM amplitude response to an AC varying tip bias, data points and their fit.

Starting from the response of the crystal to the external electric field, it was possible to extract the value of its d_{33} component. Figure 3.10 shows, as was done for the *P(VDF-TrFE)*, the mean value of the tip oscillation for each AC bias to the tip, with errors referring to the standard deviation. From this the d_{33} value is computed throughout Function 3.3, using this time d_{33} as a fitting parameter and keeping the sensitivity S as the one obtained from the *P(VDF-TrFE)* analysis. Throughout this procedure, the value we obtained was $d_{33} = 10.36 \pm 0.03 pm/V$. This value results a bit larger than the literature one of $15 \pm 2\ pm/V$, but still in the same order of magnitude. This concludes our investigations on ZnO.

3.3 ZnSnO₃
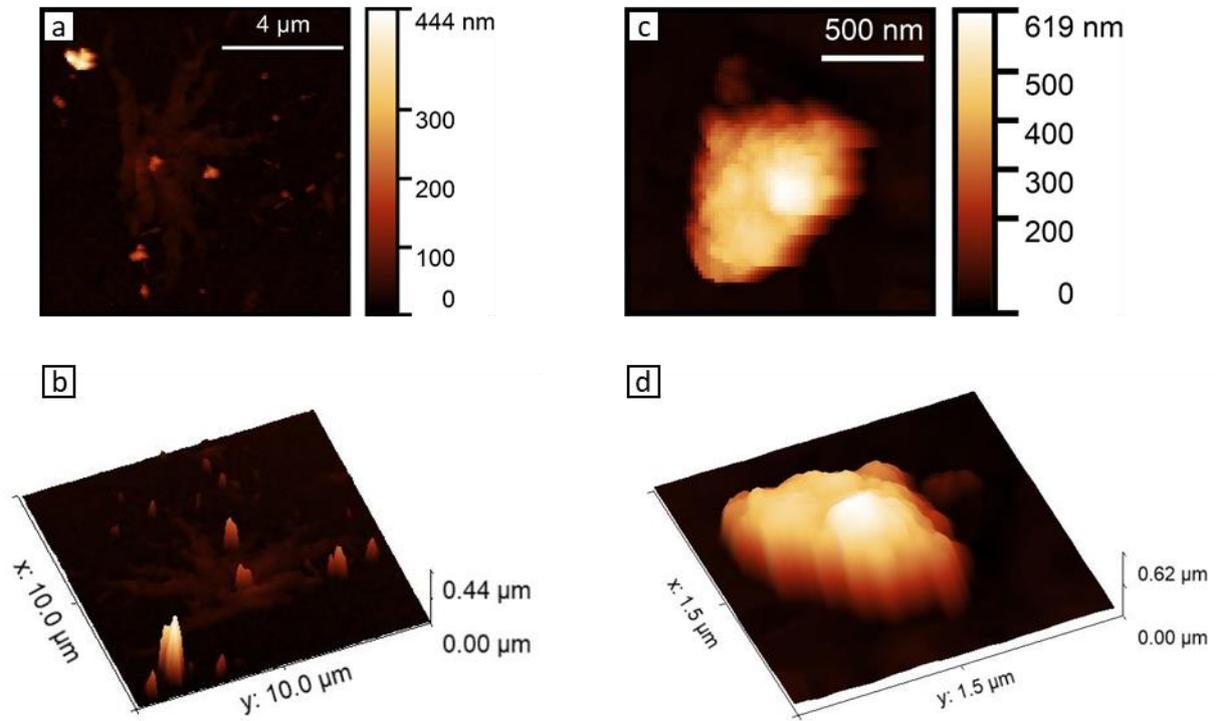
Figure 3.11: investigations of ZnSnO₃ by non-contact mode force microscopy. a, b) Topography and not to scale three-dimensional representation of the sample surface; c, d) topography and not to scale three-dimensional representation of a ZnSnO₃ structure.

Once the value of the d_{33} of the ZnO was computed, the next step of our analysis was the one of the ZTO. Figure 3.11 shows a $10\mu m \times 10\mu m$ scan of the surface where the ZTO structures were deposited. A three-dimensional representation is also provided in 3.8b. As for the ZnO, the choice for the tip was made in order to perform in Non-Contact mode and avoid damages of the sample. On this turn the choice was on a $NSC36/Cr - Au\ I$. From the scanned area, the structure exposed in Figure 3.11c was chosen for the following PFM analysis. As evident from the three-dimensional representation offered in Figure 3.11d, the structure occupies an almost cubic volume with a side of about $500 - 600nm$. Nevertheless, from a visive analysis its edges do not result sharp as were the ones of ZnO. Furthermore, its surface presents huge inequalities.

These observations led us to speculate the structure being an agglomerate of smaller sub-structures rather than a well-defined solid crystal.
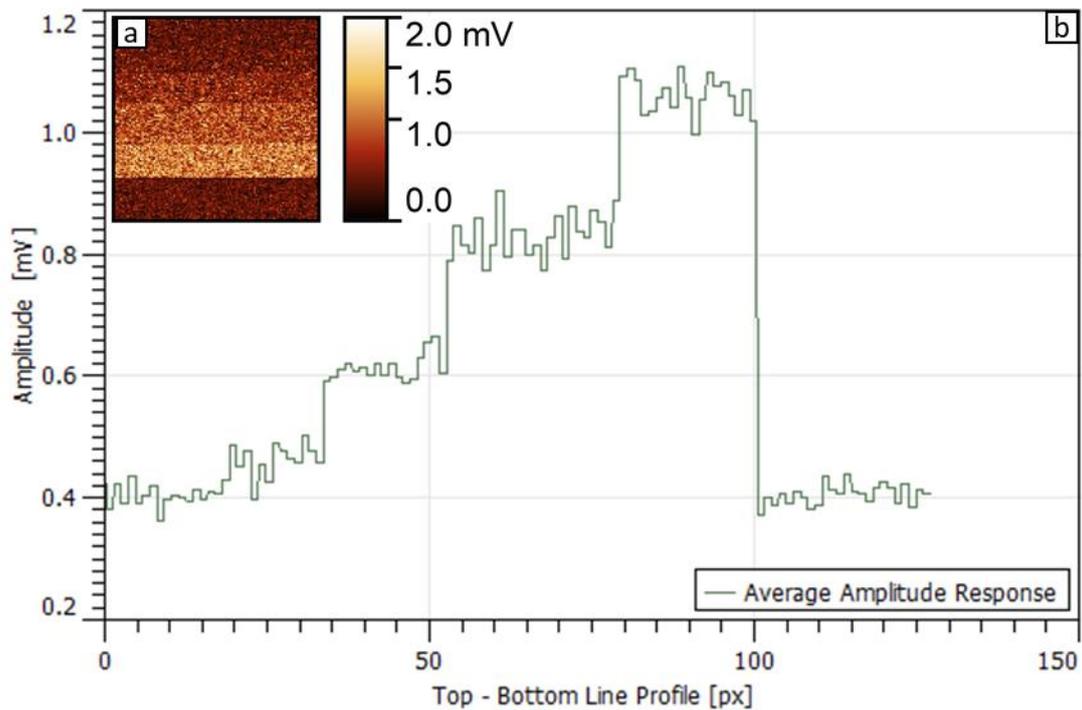
Figure 3.12: a) PFM Amplitude response to a varying bias of a single point of the ZTO crystal, b) top-bottom horizontally averaged cross section of the PFM Amplitude response.

Once the suitable structure was selected, the probe was landed on a single point of the surface in order to proceed with the PFM investigation. As was done for *P(VDF-TrFE)* and *ZnO*, an AC bias of 0, 1, 2, 3, 4, 0V was applied to the tip. Each pixel of Figure 3.12 codifies the results of this procedure. The response of the sample surface to the stimuli is plotted in figure 3.12b as the top-bottom cross-section of the values reported in Figure 3.9a averaged on horizontal lines. As for the previous samples, an increasing bias leads to an increasing PFM amplitude response. As before, this is an evidence of the piezoelectric behaviour of the structure. Also in this case, because of the background noise, to a non-null bias does not correspond a null amplitude.

Starting from the response of the structure to the external electric field, it was possible to extract the value of its d_{33} component. Figure 3.13 shows, as was done for the *P(VDF-TrFE)* and the *ZnO*, the mean value of the tip oscillation for each AC bias to the tip, with errors referring to

the standard deviation. From this, the d_{33} value is computed throughout Function 3.3, using this time d_{33} as a fitting parameter and keeping the sensitivity S as the one obtained from the *P(VDF-TrFE)* analysis. Throughout this procedure, the value we obtained was $d_{33} = 23.70 \pm 0.04 pm/V$.

Figure 3.13: ZTO crystal. Average PFM amplitude response to an AC varying tip bias, data points and their fit.

Figure 3.14 then shows the comparison between the data of the ZnO and $ZnSnO_3$ structure. As evident, the latter material is more responsive than the former.

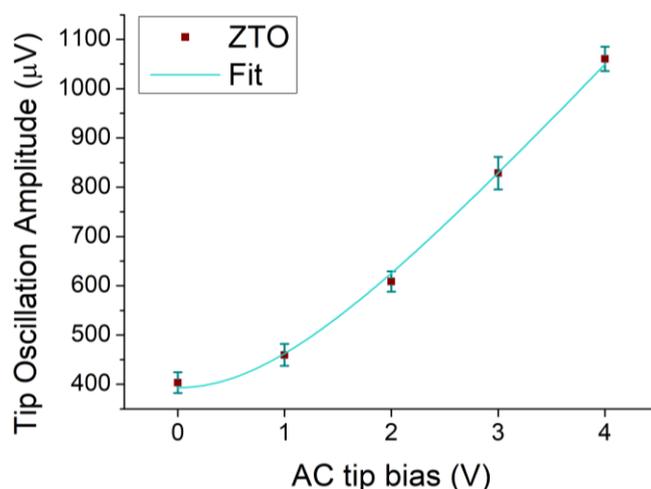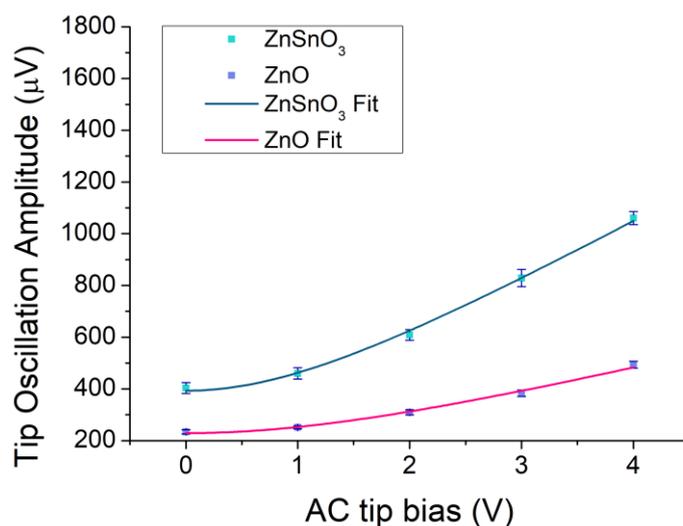*Figure 3.13: ZTO crystal. Average PFM amplitude response to an AC varying tip bias, data points and their fit.*

Conclusions

In this thesis piezoelectricity in nanowires of ZnO and $ZnSnO_3$ is investigated. As detailed in Chapter 1, piezoelectricity arises from the reorientation of the dipole moments in non-centre symmetrical crystals under the action of strain or electrostatic field. One of the most fruitful applications of piezoelectric materials is that of energy harvesting[6,7,21,49–51]. By exploiting the electric fields generated by these materials under mechanical stress, it could be possible to power devices such as medical implants[6], smart clothes or new sensors that do not require power cables or battery changes. A recent electromechanical energy harvesting device has been developed at NOVA University of Lisbon. It exploits a composite of a silicone elastomer with ZnO or $ZnSnO_3$ based nanowires. Here I performed Atomic Force Microscopy experiments to characterize such nanowires and to determine their piezoelectric response. I start my experiments with characterizations of a well characterized polymeric piezoelectric thin film, namely polyvinylidene fluoride trifluoroethylen (PVDF-TRFE). First, the topography of the PVDF-TrFE was first obtained. Using Piezoelectric Force Microscopy scan it was then observed that PVDF-TrFE has various Weiss domains, which were more reactive to electrical stress thanks to their consistently oriented dipole moments. In addition, it was verified that with a bias of 10V it is possible to completely polarize the surface of the sample, in both signs. The deformation of a single point under a PFM performed with a varying bias led to the determination of the sensitivity of the instrument. This value, that is $S = 10.4 \pm 0.1 V/\mu m$, was obtained through the fit with Equation 3.3, in which was used the value of $d_{33} = -38 pm/V$, as known from the literature. Once the sensitivity value was obtained, both samples of ZnO and $ZnSnO_3$, were scanned in Non-Contact mode for topography and PFM for the evaluation of their piezoelectric properties. The d_{33} measured for the ZnO structure is $10.36 \pm 0.03 pm/V$, which is smaller than the one taken from literature, viz $15 \pm 2 \, pm/V$, although they are still in the same order of magnitude. On the other hand, the d_{33} measured for the $ZnSnO_3$ structure is $23.70 \pm 0.04 pm/V$. The d_{33} value for the $ZnSnO_3$ results to be double that the one for the ZnO, and this is an index that it could be a good candidate for the development of further energy harvesting devices.

Bibliography

(1)   Zhao, Y.; Deng, P.; Nie, Y.; Wang, P.; Zhang, Y.; Xing, L.; Xue, X. Biomolecule-Adsorption-Dependent Piezoelectric Output of ZnO Nanowire Nanogenerator and Its Application as Self-Powered Active Biosensor. *Biosens. Bioelectron.* **2014**, *57*, 269–275. https://doi.org/10.1016/j.bios.2014.02.022.

(2)   Zhao, Y.; Lai, X.; Deng, P.; Nie, Y.; Zhang, Y.; Xing, L.; Xue, X. Pt/ZnO Nanoarray Nanogenerator as Self-Powered Active Gas Sensor with Linear Ethanol Sensing at Room Temperature. *Nanotechnology* **2014**, *25* (11). https://doi.org/10.1088/0957-4484/25/11/115502.

(3)   Deen, M.; Wielandt, E.; Stutzmann, E.; Crawford, W.; Barruol, G.; Sigloch, K. First Observation of the Earth's Permanent Free Oscillations on Ocean Bottom Seismometers. *Geophys. Res. Lett.* **2017**, *44* (21), 10,988-10,996. https://doi.org/10.1002/2017GL074892.

(4)   Zhu, G.; Yang, R.; Wang, S.; Wang, Z. L. Flexible High-Output Nanogenerator Based on Lateral ZnO Nanowire Array. *Nano Lett.* **2010**, *10* (8), 3151–3155. https://doi.org/10.1021/nl101973h.

(5)   Wang, Z. L. FUNCTIONAL OXIDE NANOBELTS: Materials, Properties and Potential Applications in Nanosystems and Biotechnology. *Annu. Rev. Phys. Chem.* **2004**, *55* (1), 159–196. https://doi.org/10.1146/annurev.physchem.55.091602.094416.

(6)   Dakua, I.; Afzulpurkar, N. Piezoelectric Energy Generation and Harvesting at the Nano-Scale: Materials and Devices. *Nanomater. Nanotechnol.* **2013**, *3*, 1. https://doi.org/10.5772/56941.

(7)   Rahman, W.; Garain, S.; Sultana, A.; Ranjan Middya, T.; Mandal, D. Self-Powered Piezoelectric Nanogenerator Based on Wurtzite ZnO Nanoparticles for Energy Harvesting Application. *Mater. Today Proc.* **2018**, *5* (3), 9826–9830. https://doi.org/10.1016/J.MATPR.2017.10.173.

(8)   Rovisco, A.; Santos, A.; Cramer, T.; Martins, J.; Branquinho, R.; Fortunato, E.; Martins,

R.; Igreja, R.; Barquinha, P. Piezoelectricity Enhancement of Nanogenerators Based on PDMS and ZnSnO 3 Nanowires Through. 1–28.

(9)   Uchino, K. The Development of Piezoelectric Materials and the New Perspective. In *Advanced Piezoelectric Materials: Science and Technology*; Elsevier Inc., 2010; pp 1–85. https://doi.org/10.1533/9781845699758.1.

(10)   Xie, X. *High-Performance Micro Actuators for Tactile Displays*; 2017. https://doi.org/10.13140/RG.2.2.31191.16806.

(11)   Katzir, S. Who Knew Piezoelectricity? Rutherford and Langevin on Submarine Detection and the Invention of Sonar. *Notes Rec. R. Soc.* **2012**, *66* (2), 141–157. https://doi.org/10.1098/rsnr.2011.0049.

(12)   Ushijima, T.; Kumakawa, S. Active Engine Mount with Piezo-Actuator for Vibration Control. In *SAE Technical Papers*; 1993. https://doi.org/10.4271/930201.

(13)   Sharma, T.; Je, S. S.; Gill, B.; Zhang, J. X. J. Patterning Piezoelectric Thin Film PVDF-TrFE Based Pressure Sensor for Catheter Application. *Sensors Actuators, A Phys.* **2012**, *177*, 87–92. https://doi.org/10.1016/j.sna.2011.08.019.

(14)   Tressler, J. F. Piezoelectric Transducer Designs for Sonar Applications. In *Piezoelectric and Acoustic Materials for Transducer Applications*; Springer US, 2008; pp 217–239. https://doi.org/10.1007/978-0-387-76540-2_11.

(15)   Nafea, M.; Nawabjan, A.; Mohamed Ali, M. S. A Wirelessly-Controlled Piezoelectric Microvalve for Regulated Drug Delivery. *Sensors Actuators, A Phys.* **2018**, *279*, 191–203. https://doi.org/10.1016/j.sna.2018.06.020.

(16)   Sodano, H. A.; Inman, D. J.; Park, G. Comparison of Piezoelectric Energy Harvesting Devices for Recharging Batteries. https://doi.org/10.1177/1045389X05056681.

(17)   Vijaya, M. S. *Piezoelectric Materials and Devices*; CRC Press, 2016. https://doi.org/10.1201/b12709.

(18)   Purcell, E. M.; Morin, D. J. *Purcell E.M., Morin D.J. Electricity and Magnetism*; Cambridge University Press, 2013.

(19)   Griffiths, D. J. Introduction to Electrodynamics. **1999**.

(20)   Mukti Nath Gupta, S. and S. K. Y. Electricity Generation Due to Vibration of Moving Vehicles Using Piezoelectric Effect. *Adv. Electron. Electr. Engeneering* **2014**, *4*, 3313–3318.

(21)   Wan, C.; Bowen, C. R. Multiscale-Structuring of Polyvinylidene Fluoride for Energy Harvesting: The Impact of Molecular-, Micro- and Macro-Structure. *J. Mater. Chem. A* **2017**, *5* (7), 3091–3128. https://doi.org/10.1039/C6TA09590A.

(22)   Harrison, J. S.; Ounaies, Z. Piezoelectric Polymers. *Encyclopedia of Polymer Science and Technology*. July 15, 2002. https://doi.org/doi:10.1002/0471440264.pst427.

(23)   Marutake, M. The Days When Piezoelectric PVDF Was Discovered. *Ferroelectrics* **1995**, *171* (1), 5–6. https://doi.org/10.1080/00150199508018416.

(24)   Bauer, S.; Bauer, F.; Heywang, W.; Lubitz, K.; Wersing, W. Piezoelectric Polymers and Their Applications. In *Piezoelectricity: Evolution and Future of a Technology*; 2008; Vol. 114, pp 157–177. https://doi.org/10.1007/978-3-540-68683-5_6.

(25)   Harrison, J. S.; Ounaies, Z.; Bushnell, D. M. *Piezoelectric Polymers*; 2001.

(26)   Li, Q.; Wang, Q. Ferroelectric Polymers and Their Energy-Related Applications. *Macromol. Chem. Phys.* **2016**, *217* (11), 1228–1244. https://doi.org/10.1002/macp.201500503.

(27)   Kawai, H. The Piezoelectricity of Poly (Vinylidene Fluoride). *Jpn. J. Appl. Phys.* **1969**, *8* (7), 975–976. https://doi.org/10.1143/jjap.8.975.

(28)   Wong, C. P. *Piezoelectric AndPyroelectric Polymers*; 1993.

(29)   Omote, K.; Ohigashi, H.; Koga, K. Temperature Dependence of Elastic, Dielectric, and Piezoelectric Properties of "single Crystalline'' Films of Vinylidene Fluoride Trifluoroethylene Copolymer. *J. Appl. Phys.* **1997**, *81* (6), 2760–2769. https://doi.org/10.1063/1.364300.

(30)   Schmidt-Mende, L.; MacManus-Driscoll, J. L. ZnO - Nanostructures, Defects, and

Devices. *Mater. Today* **2007**, *10* (5), 40–48. https://doi.org/10.1016/S1369-7021(07)70078-0.

(31)   Lee, K. Y.; Gupta, M. K.; Kim, S. W. Transparent Flexible Stretchable Piezoelectric and Triboelectric Nanogenerators for Powering Portable Electronics. *Nano Energy* **2015**, *14*, 139–160. https://doi.org/10.1016/j.nanoen.2014.11.009.

(32)   Liu, J.; Fei, P.; Song, J.; Wang, X.; Lao, C.; Tummala, R.; Wang, Z. L. Carrier Density and Schottky Barrier on the Performance of DC Nanogenerator. *Nano Lett.* **2008**, *8* (1), 328–332. https://doi.org/10.1021/nl0728470.

(33)   Rovisco, A.; Branquinho, R.; Martins, J.; Oliveira, M. J.; Nunes, D.; Fortunato, E.; Martins, R.; Barquinha, P. Seed-Layer Free Zinc Tin Oxide Tailored Nanostructures for Nanoelectronic Applications: Effect of Chemical Parameters. *ACS Appl. Nano Mater.* **2018**, *1* (8), 3986–3997. https://doi.org/10.1021/acsanm.8b00743.

(34)   Guo, R.; Guo, Y.; Duan, H.; Li, H.; Liu, H. Synthesis of Orthorhombic Perovskite-Type ZnSnO3 Single-Crystal Nanoplates and Their Application in Energy Harvesting. *ACS Appl. Mater. Interfaces* **2017**, *9* (9), 8271–8279. https://doi.org/10.1021/acsami.6b16629.

(35)   Wu, J. M.; Xu, C.; Zhang, Y.; Wang, Z. L. Lead-Free Nanogenerator Made from Single ZnSnO3 Microbelt. *ACS Nano* **2012**, *6* (5), 4335–4340. https://doi.org/10.1021/nn300951d.

(36)   Zinc Oxide Nanowire https://www.acsmaterial.com/news-detail/zinc-oxide-nanowire.html (accessed Nov 18, 2019).

(37)   Rovisco, A.; Branquinho, R.; Martins, J.; Fortunato, E.; Martins, R.; Barquinha, P. Growth Mechanism of Seed-Layer Free ZnSnO 3 Nanowires : Effect of Physical Parameters. **2019**, 37–41.

(38)   Ming Wu, J.; Xu, C.; Zhang, Y.; Lin Wang, Z. Lead-Free Nanogenerator Made from Single ZnSnO 3 Microbelt. **2012**. https://doi.org/10.1021/nn300951d.

(39)   Wang, X.; Song, J.; Liu, J.; Zhong, L. W. Direct-Current Nanogenerator Driven by

Ultrasonic Waves. *Science (80-.).* **2007**, *316* (5821), 102–105. https://doi.org/10.1126/science.1139366.

(40) Park, K.-I.; Jeong, C. K.; Kim, N. K.; Lee, K. J. Stretchable Piezoelectric Nanocomposite Generator. *Nano Converg.* **2016**, *3* (1). https://doi.org/10.1186/s40580-016-0072-z.

(41) Broitman, E.; Soomro, M. Y.; Lu, J.; Willander, M.; Hultman, L. Nanoscale Piezoelectric Response of ZnO Nanowires Measured Using a Nanoindentation Technique. *Phys. Chem. Chem. Physics-PCCP* **2013**, *26* (15), 11113–11118. https://doi.org/10.1039/c3cp50915j.

(42) Park Systems Corporation. Nx10 User ' S Manual. **2015**.

(43) Atomic Force Microscopy (AFM) http://www.nanophys.kth.se/nanophys/facilities/nfl/afm/icon/bruker-help/Content/SPM Training Guide/Atomic Force Microscopy (AFM)/Atomic Force Microscopy (AFM).htm (accessed Nov 21, 2019).

(44) Magonov, S. N.; Whangbo, M. H. *Surface Analysis with STM and AFM: Experimental and Theoretical Aspects of Image Analysis*; Wiley Blackwell, 2007. https://doi.org/10.1002/9783527615117.

(45) ElectriMulti75-G AFM Probe - BudgetSensors https://www.budgetsensors.com/force-modulation-afm-probe-platinum-electrimulti75 (accessed Nov 21, 2019).

(46) AFM Probe HQ:NSC36/Cr-Au - MikroMasch https://www.spmtips.com/afm-tip-hq-nsc36-cr-au (accessed Nov 21, 2019).

(47) Rovisco, A.; Branquinho, R.; Martins, J.; Oliveira, M. J.; Nunes, D.; Fortunato, E.; Martins, R.; Barquinha, P. Seed-Layer Free Zinc Tin Oxide Tailored Nanostructures for Nanoelectronic Applications: Effect of Chemical Parameters. *ACS Appl. Nano Mater.* **2018**, *1* (8), 3986–3997. https://doi.org/10.1021/acsanm.8b00743.

(48) FrancescoCalavalle. Electrospun Nanofibers for Investigated By Scanning Probe Microscopy. **2016**.

(49) Sun, C.; Shi, J.; Bayerl, D. J.; Wang, X. PVDF Microbelts for Harvesting Energy from

Respiration. *Energy Environ. Sci.* **2011**, *4* (11), 4508–4512. https://doi.org/10.1039/C1EE02241E.

(50)   Maurya, D.; Yan, Y.; Priya, S. J. Piezoelectric Materials for Energy Harvesting; 2015; pp 143–178. https://doi.org/10.1201/b18287-6.

(51)   Wan, C.; Bowen, C. R. Multiscale-Structuring of Polyvinylidene Fluoride for Energy Harvesting: The Impact of Molecular-, Micro- and Macro-Structure. *Journal of Materials Chemistry A*. Royal Society of Chemistry 2017, pp 3091–3128. https://doi.org/10.1039/c6ta09590a.